

INVESTIGATION OF NEW CHEVREL PHASE
COMPOUNDS FOR IMPROVED EFFICIENCY OF
THERMOELECTRIC POWER GENERATION DEVICES

A Thesis

Presented to the Faculty of the Graduate School
of Cornell University

in Partial Fulfillment of the Requirements for the Degree of
Master of Science

by

Anneliese Marin Schmidt

August 2005

© 2005 Anneliese Marin Schmidt

ALL RIGHTS RESERVED

ABSTRACT

In the search for improved high-temperature thermoelectric materials, we investigate new Chevrel phase materials that combine substitution of *Ru* on some of the *Mo* sites and the intercalation of various metals into the Chevrel structure. We expect these materials to have low thermal conductivities, due to their rattling structure type. Nominal compositions are (generally) chosen to add 4 valence electrons to the basic Chevrel unit Mo_6Se_8 , and make the structure semiconducting. Two series of compounds were synthesized, $(Cu_yMo_6Se_8)_{1-x}(Mo_4Ru_2Se_8)_x$, with $y = 2, 4$ and $x \approx 0, 0.2, 0.4, 0.6, 0.8$, and $M_xMo_5RuSe_y$, with $M = Zn, Cd, Sn$ and Pb , $x \lesssim 1$, and $y \approx 8$. These generally differ from loading stoichiometry, and only a few were found to be intrinsic semiconductors. For the first series we report the synthesis and transport property measurements, and for the latter we present the synthesis and characterization of each compound. Since nearly all previous studies of Chevrel phase compounds have exclusively involved either substitution or intercalation, this research is an important addition to the study of Chevrel phase compounds.

BIOGRAPHICAL SKETCH

I was born in Kentfield, CA on July 14th, about 20 minutes before my sister, Vanessa. This was quite a surprise for my parents. I grew up in Marin county, surrounded by beautiful hills and nature that I didn't learn to appreciate fully until I moved away for college. I graduated from University of Arizona in May 2003, with a B.S. in Physics and Astronomy (and minors in Mathematics and Spanish). Above the obvious academic merits, I was excited to come to Cornell for trees and other green things, fireflies, and seasons. I now look forward to move somewhere with less drastic temperature variations (eventually). I am moving to the Washington D.C. area, to find a job in alternative energy.

ACKNOWLEDGEMENTS

First, I would like to thank my advisor, Frank DiSalvo, for all his help and explanations, and for his extraordinary kindness and optimism. And thank you to Michael McGuire, for your guidance, and patience with my constant questions. Its not your fault I'm leaving, you've been a great teacher and friend.

I thank all of my family for their continued support and belief in me - Mom, Dad, Vanessa, Joe, Tammy, Omar. Thank you to Ken Weaver, for being a good reason to get up every morning. And for help with LaTeX. I thank Steve, for understanding me, for being more appetizing to mosquitos than I am, and for (way too many) pancakes. And thanks to Luna for being furry and cute.

I would also like to thank the rest of the DiSalvo group, who are tremendously generous with their time and help, very friendly, and always amusing.

Finally, I thank Cornell for financial support, and for being a great place to learn.

TABLE OF CONTENTS

1	Introduction to Thermoelectrics: theory and devices	1
1.1	History and Background	5
1.2	Thermoelectric theory from Transport Phenomena	7
1.2.1	Irreversible effects	8
1.2.2	Reversible effects	9
1.3	Thermoelectric Theory from Irreversible Thermodynamics	11
1.4	Device Equations	13
1.4.1	TE power generation device	14
1.4.2	TE Power Generator Efficiency and Figure of Merit	16
1.5	What Makes a “Good” Thermoelectric?	19
1.5.1	Optimizing the basic parameters of ZT	19
1.5.2	Optimizing the materials properties	25
1.6	Chevrel Phases	30
	References	40
2	Synthesis and Thermoelectric properties of $(Cu_yMo_6Se_8)_{1-x}(Mo_4Ru_2Se_8)_x$	43
2.1	Motivation and review	43
2.2	Experimental	45
2.2.1	Reagents	45
2.2.2	Sample preparation	45
2.2.3	Powder X-Ray diffraction analysis	46
2.2.4	Transport property measurements	47
2.2.5	Microprobe analysis	48
2.3	Results and Discussion	49
2.3.1	Measured Compositions	49
2.3.2	Powder X-ray diffraction analysis	52
2.3.3	Transport property measurements	54
2.4	Conclusions	57
2.5	Acknowledgments	58
	References	61
3	Synthesis and Characterization of $M_xMo_5RuSu_8$ Chevrel Phase compounds	63
3.1	Motivation and review	63
3.2	Experimental analysis	65
3.2.1	Reagents	65
3.2.2	Sample preparation	65
3.2.3	Powder X-ray diffraction analysis	67
3.2.4	Microprobe analysis	68

3.2.5	Rietveld refinement	69
3.3	Results and Discussion	69
3.3.1	Measured compositions	69
3.3.2	Mo_5RuSe_8 structure	72
3.3.3	Rietveld refinement	73
3.3.4	Crystal structures	80
3.3.5	Cluster metal and selenium bonds	82
3.4	Conclusions	85
3.5	Acknowledgments	86
	References	87
4	Conclusion	89

LIST OF TABLES

2.1	Measured compositions (high-precision microprobe analysis) and unit cell parameters (powder XRD)	51
3.1	Refined M occupancy, unit cell parameters, conventional reliability factors, and weight % $MoSe_2$ from the Rietveld method	75
3.2	Positions (x, y, z) and isotropic thermal parameters (B_{iso}) from Rietveld refinement, and atomic ratios from microprobe analysis . .	78
3.3	Selected bond lengths (in Å)	83

LIST OF FIGURES

1.1	Schematic diagrams of thermoelectric (a) power generation and (b) refrigeration devices.	4
1.2	A schematic view of a simple TE circuit	9
1.3	Thermoelectric FOM as a function of temperature for the best thermoelectric materials	20
1.4	This schematic graph of S^2 , σ , and $1/\kappa$ as a function of charge carrier density	21
1.5	$PbMo_6Se_8$ Chevrel phase unit	32
1.6	Extended structure of Chevrel phase Mo_6Se_8 unit	33
1.7	Large cavity formed by packing of Chevrel clusters	34
1.8	Three cavities formed by packing of Chevrel clusters	35
1.9	Calculated DOS for Mo_6Se_8	37
1.10	Band structure of Mo_6Se_8	38
2.1	Powder XRD patterns for series 1 alloys	53
2.2	Powder XRD patterns for series 2 alloys	54
2.3	Resistivity as a function of temperature for series 1 compounds.	55
2.4	Resistivity as a function of temperature for series 2 compounds	56
2.5	Seebeck coefficient as a function of temperature for series 1 compounds.	57
2.6	Seebeck coefficient as a function of temperature for series 2 compounds	58
2.7	Resistivity and Seebeck coefficient as a function of temperature for $Mo_4Ru_2Se_8$	59
2.8	Calculated Power Factor as a function of temperature for (a) series 1 and (b) series 2	60
3.1	Powder XRD pattern of $Mo_5RuSe_{7.7}$	72
3.2	Powder patterns for a) $ZnMo_5RuSe_8$, b) $CdMo_5RuSe_8$ c) $SnMo_5RuSe_8$, and d) $PbMo_5RuSe_8$ (nominal compositions).	74
3.3	$CdMo_5RuSe_8$ structure	80
3.4	$(Sn/Pb)Mo_5RuSe_8$ structure	81
3.5	Intracluster Mo-Mo bonds	84

CHAPTER 1
**INTRODUCTION TO THERMOELECTRICS: THEORY AND
DEVICES**

The flood of technological development during the 21st century has had a huge impact on this planet. Although it has led to numerous positive changes in our health and comfort and created unparalleled opportunities for science and discovery, not all of the consequences of this technological revolution have been beneficial. One of the more dire problems our world faces today is the fast-paced degradation of the environment, which seems to be primarily a result of human action. As a result, there has been a surge of public concern and increasing interest in the environment, as well as much scientific research focused on how to understand and amend the problem. One of the biggest concerns we face is the increasing threat of global warming and air pollution, which are both significantly worsened by the widespread use of fossil fuels as our main energy source. This has triggered research in a wide range of possible sustainable energy sources. Added to the environmental concern is the increasing price of fossil fuels and the decreasing availability of this non-renewable energy source. Many different types of renewable energy sources are now being explored, and there is much effort to develop new technologies that take advantage of unharnessed power sources.

One such possibility is using thermoelectric (TE) devices for power generation. These devices make use of excess heat, including waste heat, by turning it into a usable power source. The current problem with such devices is their low efficiency, which makes them economically uncompetitive with current energy sources. However, if a new TE material was developed that had a higher efficiency, there would be a large market ready to incorporate them into everyday use.

In addition to power generation, TE devices can be also be designed for active cooling (refrigeration) or heat generation, although the same efficiency problem arises in these applications. Since the efficiency of a TE material depends on the temperature at which it operates, the search for good low-temperature TE materials for refrigeration and high-temperature materials for power generation need to be conducted separately. However, an efficient TE refrigeration device that could replace compressed-gas based home refrigerators would have important environmental benefits as well.

At a very basic level, the term *thermoelectric* describes the relationship between heat gradients and electric current in a material or in the junction of two different materials. The strength of this relation depends upon a variety of transport phenomena, each of which are directly influenced by the inherent properties of the material. The five main transport phenomena include irreversible Joule heating and thermal conduction, and reversible Seebeck, Peltier, and Thompson effects. These will be discussed in detail in section 1.2. The main property used to characterize thermoelectrics is the dimensionless figure of merit, $ZT = \frac{\sigma S^2 T}{\kappa}$, where σ is the electrical conductivity, S is the Seebeck coefficient or thermopower, T is the temperature, and κ is the thermal conductivity. This term will be thoroughly discussed in section 1.4.2. The figure of merit (FOM) appears in equations describing both the efficiency of a thermoelectric power generator and the coefficient of performance (COP) of a thermoelectric refrigerator, and needs to be maximized for improved devices. The main focus of TE research is to increase ZT .

We can use the FOM to quantify the amount of improvement required for TE devices to become competitive with current technologies. In order to compete with compressed-gas based home refrigerators which have a COP of about 30% of the

Carnot limit, a TE material would need to have a $ZT \sim 4$ [1]. Unfortunately, even the best TE refrigeration materials available today only have $ZT \sim 1$ (at room temperature). Similar efficiencies are found in high-temperature TE devices. Many materials scientists have recently realized the extreme challenges inherent in finding a low-temperature TE that could be used to replace home refrigerators [2], but they have higher hopes for finding a good high-temperature TE. As a result, most current thermoelectric research is focused on high-temperature materials. Since this includes the research presented in this thesis, we focus primarily on high-temperature thermoelectric theory and minimize the discussion of low-temperature thermoelectrics.

But before delving into a thorough discussion of thermoelectric theory, it is useful to first introduce the two basic thermoelectric devices. A schematic diagram in Figure 1.1 shows a TE power generation device (a) and a refrigeration device (b). These devices are very similar, each containing slabs of p-type (positive charge carriers) and n-type (negative charge carriers) thermoelectric materials sandwiched in-between a heat source and a heat sink. This arrangement creates a temperature gradient across the samples. An electronically conducting plate is connected across the p-n junction so that current can flow through the circuit. It is primarily the direction of current flow that dictates whether it is a power generation or refrigeration device. In the power generation device, the temperature gradient causes the charge carriers to move from the heat source to the heat sink, inducing a current flow which can be used to generate power. Conversely, the refrigeration device uses an input current to drive charge carriers from the cold end to the hotter end, which transfers heat and actively cools the already colder top plate. Although real devices are generally more complicated, sometimes with

several stages operating at different temperatures, this diagram serves to illustrate the basic guiding principles for thermoelectric devices.

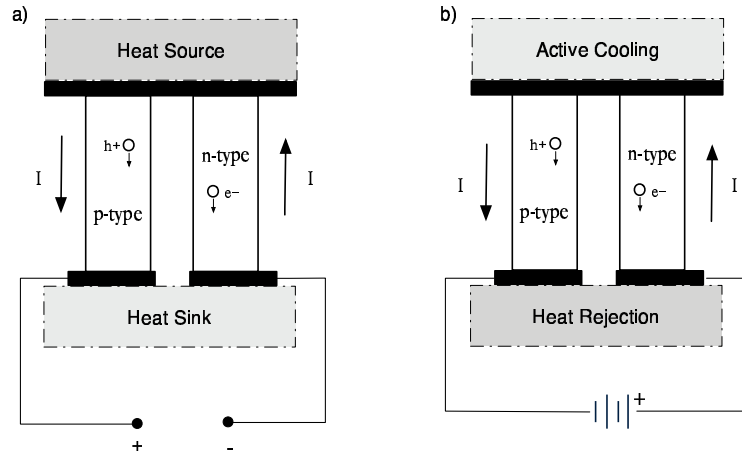


Figure 1.1: Schematic diagrams of thermoelectric (a) power generation and (b) refrigeration devices. The current I flows in the circuit in the direction of the arrows, and the black slabs represent conducting plates. The terms $h+$ and $e-$ stand for holes and electrons, respectively. See text for further discussion. Figure adapted from similar figures in DiSalvo [1] and Sales [3].

It is important to note that even if we never develop thermoelectric devices that are competitive with current power generation or refrigeration technologies, there will still be niche markets for TE devices in which the need for reliability, zero vibration, or minimal weight are more important than high efficiencies. Currently, thermoelectrics usage ranges from refrigeration in portable picnic coolers that can be powered from a car battery [1] to thermoelectric generators which generate power on unmanned space probes. In fact, Radioisotope Thermoelectric Generators (RTG's), which use radioactive isotopes to produce the heat source for the TE power generation, have been used for decades in spacecraft like the Voyager and Pioneer [4]. In these types of markets where TE materials are already useful, even small improvements in the materials' efficiencies will be a great help.

Although the search for a “good” thermoelectric is not a new one, there are

reasons to believe it is possible to create an efficient TE material. The requirements for such a material will be discussed in detail in section 1.5. There have been several encouraging reviews published in the last decade that illustrate this search and are optimistic about the eventual success of the research [1, 3, 5]. Although finding a good thermoelectric has so far proven to be a difficult task, the possible economic and environmental rewards for developing such a material make the search worth the effort.

Having presented some motivation for TE research and introduced the basic ideas behind TE devices, we can now proceed to explain the science of thermoelectrics. We will begin with a brief review of the history of thermoelectrics. Then, the theory of thermoelectrics from both transport phenomena and irreversible thermodynamics will be considered, followed by a more rigorous description of thermoelectric devices and derivation of the main device equations. Using this foundation of TE theory, we will outline what makes a “good” thermoelectric, defining the main materials properties that improves the thermoelectric figure of merit. Finally, we will describe Chevrel phases, the particular class of TE materials that is the focus of this research, and explain why they are expected to be good high temperature thermoelectrics.

1.1 History and Background

The study of thermoelectrics has been going on for nearly two centuries. It began in 1822, when Thomas Seebeck noticed there was a potential difference across the junction of two different materials which were held at different temperatures [6]. Although he was unable to accurately describe the reason for this effect, his discovery was crucial to the development of thermoelectrics. More than ten

years after Seebeck's observation, Jean Peltier discovered the reverse process: an electrical current being used to create a temperature gradient across the junction of two materials [7]. It was Peltier who first came up with the idea of using thermoelectric materials as cooling devices. Nearly 50 years later, in 1885, Lord Rayleigh realized that a similar thermoelectric device could be used to generate power, and (inaccurately) calculated the efficiency of such a device [4, 8].

Reasonable theoretical explanations of these effects were first discussed by Thomson (Lord Kelvin) in 1851, after the advent of reversible thermodynamics [9]. He was also able to find a simple mathematical relation between the Seebeck (S) and Peltier (π) coefficients, such that $\pi = S \cdot T$, where T is the temperature of the material. Kelvin also predicted and observed another important thermoelectric process, now called the Thomson effect, which accounts for the exchange of heat between a material and its surroundings when there is both a temperature gradient across the material and a current flowing through it.

With time, thermoelectric theory developed further, and by the early 1900's Altenkirch had derived a reasonable theory of TE power generation and refrigeration [4]. Furthermore, with the development of irreversible thermodynamics, Onsager proved that Kelvin's assumptions in TE theory were justified, and showed that Kelvin had derived the correct relations between TE phenomena. In 1931, he published two important papers developing these ideas [10, 11].

Despite the theoretical efforts made in thermoelectrics near the beginning of the century, the experimental development was somewhat lacking due to the enormous excitement in other areas of physics at that time. Most of the TE research during that period showed little promise for ever finding a good thermoelectric. As such, experimental interest in thermoelectrics didn't develop fully until the late 1950's,

when Ioffe [8] showed that highly doped semiconductors could make more efficient TE materials. This was an encouraging development that brought new vitality to the experimental work in thermoelectrics and led to the discovery of the best low-temperature thermoelectric material to date, Bi_2Te_3 and its alloys with Sb_2Te_3 or Sb_2Se_3 .

However, after the initial burst of TE research following Ioffe's theory, interest quickly drained when thermoelectric materials better than these bismuth telluride alloys were not found. But interest in thermoelectrics has recently been revitalized with the hope that over 40 years of semiconductor research will improve the odds of finding a "good" thermoelectric. In addition to the improvements in synthesizing and characterizing new compounds, solid state theory has blossomed, leading to great improvements in the models for semiconductor systems. Although we are still unable to predict the exact properties of a ternary or quaternary compound, we are now better able to speculate which systems might work.

In the next two sections, we will introduce some of the relevant TE theory, which will later be helpful for explaining some of the requirements for TE devices and improved thermoelectric materials.

1.2 Thermoelectric theory from Transport Phenomena

Macroscopic thermoelectric theory is based on the appropriate transport effects. There are five main transport properties that underlie the thermoelectric properties of a material. As mentioned above, these include irreversible effects of Joule heating and thermal conduction, and the reversible Seebeck, Peltier, and Thomson effects. Each of these phenomena will be considered in turn. Much of this material has been written and derived following Heikes [12].

1.2.1 Irreversible effects

Both of the irreversible phenomena are common effects which are described in most general physics texts. Because of their familiarity they will not be discussed here in detail, but only briefly described. Joule heating is the resistive heating that occurs in any current carrying resistive material. Joule heating is often expressed as the power dissipated in a resistor, $P = I^2R$, where I is the electrical current and R is the resistance. We can alternately express Joule heating as the rate of flow of energy density, with units of (energy/volume/time). To do this we can write the resistance in terms of the resistivity (ρ), length (L), and cross-sectional area (A) such that $R = \frac{\rho L}{A}$. If we also write the current as a current density $J = I/A$, then we have the relation,

$$\dot{q}_{Joule} = \rho J^2. \quad (1.1)$$

It is useful to remember that ρ is equal to $1/\sigma$. The units of ρ most often used for thermoelectrics are ($\Omega \cdot cm$).

The other relevant irreversible process is thermal conduction, which describes how a temperature difference induces heat to flow from the hot end of a material to the cold end. A good discussion of heat conduction is given by Zemansky [13]. Fourier's law shows that the rate of heat flow ($\dot{Q}_{Fourier}$) is proportional to the thermal conductivity (κ) of the material and the heat gradient (∇T) across the sample. If we express this heat flow as simply an energy per unit time, this gives the relation,

$$\dot{Q}_{Fourier} = -\kappa A \nabla T. \quad (1.2)$$

Since this is not an energy density, a capital 'Q' has been used. The SI units for κ are ($W/m \cdot K$), but for TE materials thermal conductivities are often given in

terms of $(mW/cm \cdot K)$. Note that equation (1.2) is valid only when there is no current flowing in the sample.

1.2.2 Reversible effects

Figure 1.2 will be used to help explain the reversible thermoelectric effects, and to gain a better understanding of TE materials. It shows a simplified TE circuit with materials A and B, connected at a hot (T_h) and cold (T_c) junction. A potential V_o is applied across the circuit, causing a clockwise current to flow.

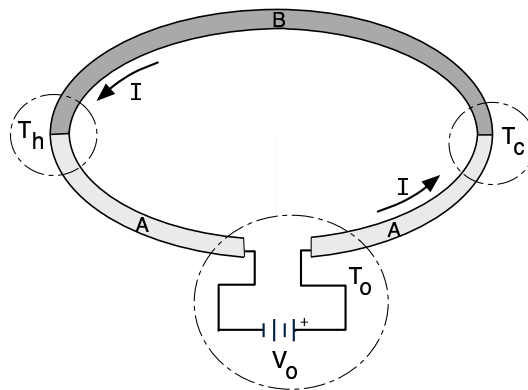


Figure 1.2: A schematic view of a simple TE circuit, with materials A and B connected at 2 junctions. The dashed circles show isothermal regions. The ends of material A are subject to applied voltage V_o and are at the same temperature, T_o . This figure is adapted from Heikes [12].

Since the Seebeck effect is the most important reversible transport phenomena for TE power generation, it will be explained first. The Seebeck effect describes the potential difference (V_{AB}) that is created across a sample when it is subject to a heat gradient. This relationship is described by the simplified equation,

$$V_{AB} = (S_A - S_B) \Delta T. \quad (1.3)$$

From this, it is clear that the units of the Seebeck coefficient (S) are (V/K) .

The Seebeck coefficient can be either positive or negative, depending on the sign of the charge carrier. By convention, the Seebeck voltage is considered to be positive if it induces a current to flow from A to B at the cold junction. Thus, if we let R be the total resistance of both materials and measure the potential drop across a junction in the circuit in Figure 1.2, it would differ from the applied voltage V_o by the Seebeck voltage, such that $IR = V_o - V_{AB}$.

The Peltier effect is the opposite of the Seebeck effect: it describes how a heat flow can be produced by an applied electric current in a material at constant temperature. The Peltier coefficient (π) is defined by the relation between the electrical current and the heat current. Thus we can write the rate of heat flow from the Peltier effect as,

$$\dot{Q}_{Peltier} = -\pi I. \tag{1.4}$$

The units for heat flow are (energy/time). The Peltier and Seebeck coefficients are related by the Thompson relation, which gives $\pi = T \cdot S$, and thus the units of π are (V). As with the Seebeck coefficient, each material has a distinct value of π . But unlike the Seebeck effect, the Peltier effect really only affects the heat flow at a junction of two materials with different π . At the hot junction in Figure 1.2, we can write $\dot{Q}_{Peltier} = -(\pi_A - \pi_B)I$. The sign convention for the Peltier effect is that a positive current is one that goes from A to B , and that $Q > 0$ implies heat is absorbed by the system. Taking into account the negative sign in equation (1.4), this implies that when current is flowing from B to A a positive π is measured, and heat will be absorbed by the system.

When current is passed through a material in which a temperature gradient exists, heat must be exchanged with the surroundings to maintain the original temperature gradient. This process is called the Thomson effect. It is the least

significant effect of all the dominant thermoelectric processes. The Thomson heat current can be written as the dot product of the current density and the temperature gradient, such that,

$$\dot{q}_{Thomson} = \tau J \cdot \nabla T, \quad (1.5)$$

where τ is the Thomson coefficient. The units of $\dot{q}_{Thomson}$ are (energy/volume/time). We can relate the Thomson and Seebeck coefficients by $\tau = T \frac{dS}{dT}$, which shows that τ has the same units as S . The sign convention for the Thomson effect is the same as with the Peltier effect, so that for $\tau > 0$ heat is absorbed by the system when the current flows from lower to higher temperature.

This completes the introduction of the main reversible and irreversible phenomena relevant to thermoelectrics. Although the discussion has been brief, it should be sufficiently detailed to understand the related TE theory that follows. For further development of these TE phenomena, refer to [4, 12, 14, 15], where they are discussed in detail. Before we plunge into the development of TE device equations, we will first present the theory of thermoelectrics from a thermodynamic standpoint.

1.3 Thermoelectric Theory from Irreversible Thermodynamics

In 1857, Lord Kelvin became the first to establish a reasonable thermoelectric theory, which was based on reversible thermodynamics [16]. Although his theory gave the correct result, it was based on the incorrect assumption of reversibility in all thermoelectric phenomena [12]. It was not until after the development of irreversible thermodynamics and the work of Onsager [10, 11] that Kelvin's ther-

moelectric theory was confirmed by more rigorous arguments. Since this is only a brief overview of TE theory, we will not describe Kelvin's theory here. In this section we instead concentrate on the development of thermoelectric theory from an irreversible thermodynamical standpoint, which was pioneered by Callen [17] and de Groot [18]. Excellent reviews of this subject have been written by Price [19] and Domenicali [20]. The derivation presented in this section generally follows that of Heikes [12].

We begin by writing a general linear relation between a flux J_i and 'forces' X_j that produce the flux,

$$J_i = \sum_{j=1}^N L_{ij} X_j, \quad (1.6)$$

where L_{ij} represents a matrix of coefficients. When this is applied to TE theory, this sum over forces becomes important in order to allow for particle flow from both heat gradients and potential differences. Onsager's critical contribution to this development was to show that if the relation between the forces and fluxes in such a linear theory can be written as

$$\theta = \sum_{i=1}^N J_i X_i, \quad (1.7)$$

where θ is the rate of internal generation of entropy, then the matrix L_{ij} is symmetric. This relation greatly simplifies the development of TE theory, as the symmetric matrix creates an obvious connection between the fluxes.

Following these ideas for fluxes given above and considering the appropriate conservation laws, we can then write the particle flux (\mathbf{J}_e) and entropy flux (\mathbf{J}_s) as,

$$\mathbf{J}_e = L_{ee}[-(1/T)\nabla\bar{\mu}] + L_{es}[T\nabla(1/T)], \text{ and} \quad (1.8)$$

$$\mathbf{J}_s = L_{se}[-(1/T)\nabla\bar{\mu}] + L_{ss}[T\nabla(1/T)], \quad (1.9)$$

where $\bar{\mu}$ is the electrochemical potential per particle and T is the temperature. The electrochemical potential is defined as $\bar{\mu} = \mu - eV$ where μ is the chemical potential, e is the charge of an electron, and V is the electric potential. For more details on this derivation please refer to Heikes [12]. Since these equations satisfy Onsager's "θ -rule," equation (1.7), we see that $L_{es} = L_{se}$.

Equations 1.8 and 1.9 are based on general irreversible thermodynamic arguments and are not yet specific to thermoelectrics phenomena. But by applying TE processes to these general equations we can constrain the coefficients in the matrix, thus establishing a useful relation for particle flux. From this we can determine the current density \mathbf{J} , since $\mathbf{J} = -e\mathbf{J}_e$. Using the definitions of $\bar{\mu}$ and S given above, the result is as follows:

$$\mathbf{J}_e = -(\sigma/e^2)(\nabla\bar{\mu} - S\nabla T), \quad (1.10)$$

$$\mathbf{J}/\sigma = (1/e)\nabla\bar{\mu} + S\nabla T. \quad (1.11)$$

We now have a relationship between electric current, voltage, and heat. These relations are critical for understanding thermoelectrics and necessary for deriving useful device equations such as those considered in the next section.

1.4 Device Equations

Next we consider some of the relevant device equations for TE materials. We focus on high-temperature devices, particularly on deriving the efficiency of a thermoelectric power generator. Derivations of COP and other parameters important for low-temperature TE devices can be found in references [2] and [12].

1.4.1 TE power generation device

We will first consider a model of a simple power generation device, following the approach of Mahan [2].

We can write the current flux, equation (1.11), in terms of the electric field $\mathbf{E} = -\nabla V$. Then we get,

$$\mathbf{J} = \sigma(\mathbf{E} - S\nabla T), \quad (1.12)$$

with units of (*current/area*). Furthermore, we can write an equation for the heat flux \mathbf{J}_Q with units of (*energy/time/area*) in terms of the current by considering the effects of thermal conduction and the Peltier effect.

$$\mathbf{J}_Q = ST\mathbf{J} - \kappa\nabla T. \quad (1.13)$$

The first term is just $\dot{Q}_{Peltier}$ from equation (1.4), divided by area A , with the substitution $\pi = ST$. And the second term is $\dot{Q}_{Fourier}$ from equation (1.2), divided by A . With these two relations we can derive a model for basic TE devices.

To simplify the argument we will limit the discussion to one-dimensional (1-D) devices. Further, we approximate S , σ , and κ to be temperature-independent constants to make the calculations more straightforward. It is important to note, however, that in real materials these parameters do exhibit some dependence on temperature.

Keeping these limitations in mind, we can write the 1-D equation of continuity for charge density ρ and current density J as,

$$\frac{\partial \rho}{\partial t} + \frac{\partial J}{\partial x} = 0, \quad (1.14)$$

where the first term is zero in steady state. Our approximations leave only three quantities that are spatially dependent: $T(x)$, $V(x)$, and $J_Q(x)$. Thus we need

three independent equations to solve for these terms. The first two equations are the 1-D versions of J and J_Q above, and the third comes from Domenicali's [24] equation for conservation of energy. This final equation is formed by setting the total change of the energy density per time equal to zero. The energy density includes the two irreversible TE effects of Joule heating and thermal conduction. (Note that in this simplified calculation we assume the contribution from the radiation of heat lost from the surface is negligible.) Thus we have,

$$0 = \rho J^2 + \kappa \nabla^2 T. \quad (1.15)$$

We can now find relations for $T(x)$, $V(x)$, and $J_Q(x)$. Consider a bar of length L with a temperature gradient such that $T(0) = T_c$ (cold), and $T(L) = T_h$ (hot). Solving equation (1.15) with these boundary conditions gives,

$$T(x) = T_c + \frac{x}{L} \Delta T + \frac{\rho J^2}{2\kappa} x(L - x), \quad (1.16)$$

where $\Delta T = T_h - T_c$. This equation can then be used to find the other two relations. Taking the derivative with respect to x ,

$$\frac{dT(x)}{dx} = \frac{\Delta T}{L} + \frac{\rho J^2}{\kappa} \left(\frac{L}{2} - x \right). \quad (1.17)$$

Plugging this directly into the 1-D version of equation (1.13), we get,

$$J_Q = SJT(x) - \frac{\kappa \Delta T}{L} - \rho J^2 \left(\frac{L}{2} - x \right). \quad (1.18)$$

Finally, we can solve for the potential using equation (1.12), by plugging in equation (1.17) and solving for E . Using the relation $V = \int E \cdot dl$, we can then solve for $V(x)$, giving,

$$V(x) = \frac{x}{L} (\rho JL + S \Delta T) + \frac{\rho S J^2}{2\kappa} x(L - x). \quad (1.19)$$

Now that we have shown the relations between J_Q , V , and T for a 1-D power generation device, we can proceed to develop the device efficiency and show its relation to the thermoelectric FOM.

1.4.2 TE Power Generator Efficiency and Figure of Merit

Next we will look closely at the figure of merit, Z , which is one of the most essential characteristics of thermoelectric materials. Since Z has units of (T^{-1}) , it is often discussed in the dimensionless form ZT . This value is important in calculating efficiencies and other device equations. Essentially, TE research is an effort to increase ZT .

Here we show how to ‘derive’ this figure of merit by considering the balance of heat flow from the hot junction of a simple thermoelectric generator, generally following ideas presented in references [2, 12, 21, 22]. We consider a power generation device as in Figure 1.1, and make the simplification that ρ , κ , and S are temperature-independent. The assumption that $S \neq S(T)$ implies the Thomson heat, $\dot{q}_{Thompson} = 0$. Thus, only three of the main TE effects need to be considered: thermal conduction, which transfers heat away from the hot junction; and the Peltier and Joule heats, which are absorbed by the hot junction. If we assume that the materials in each leg have the same S , κ , and ρ (to simplify the calculation), we can then write $\dot{Q}_{Joule} = \frac{\rho I^2 L}{A}$, $\dot{Q}_{Fourier} \approx \kappa A \nabla T$, and $\dot{Q}_{Peltier} = -\pi I$. Notice that the Fourier heat flow equation is only approximate, since there is current flowing in the circuit.

Balancing the rate of energy flow at the hot junction gives,

$$\dot{Q}_h = A(\kappa \nabla T) + \pi I - \frac{\rho I^2 L}{2A} = 0, \quad (1.20)$$

which is equal to zero in steady state since the total heat into the junction must

equal the total heat out. Here, the Joule heat at the junction has been approximated as 1/2 the Joule heat in one leg of the device. Also note that we can simplify equation (1.20) by writing ∇T as $\frac{T_h - T_c}{L}$ (which is approximately true for this 1-D analysis), $\Delta T = T_h - T_c$, and $\pi = ST_h$.

Notice that we can also get an equivalent relation from equation (1.18) for $J_Q(x)$ with $x = L$ for the hot source (at temperature T_h),

$$J_{Qh} = J_Q(L) = ST_h J - \frac{\kappa \Delta T}{L} + \frac{\rho J^2 L}{2}. \quad (1.21)$$

Next we can eliminate the electrical current from equation (1.20) by considering the sum of the voltages through the circuit. In order to produce power, the electrical current must flow through an external load resistor with resistance R_L . The voltage across this resistor ($V = IR_L$) is balanced by the potential from internal resistance in the circuit, R_{int} , and the Seebeck voltage $S\Delta T$. From this, we can write the current as,

$$I = \frac{S\Delta T}{R_L + R_{int}}. \quad (1.22)$$

To optimize the efficiency of a TE generator, $\eta = P_{out}/\dot{Q}_h$, we need to maximize the power of the thermoelectric generator $P_{out} = I^2 R_L$ with respect to R_L . Plugging in the electrical current from equation (1.22), this becomes,

$$P_{out} = \frac{S^2(\Delta T)^2 R_L}{(R_L + R_{int})^2}. \quad (1.23)$$

We maximize P_{out} by taking the derivative with respect to R_L and setting it equal to zero, such that,

$$\frac{dP_{out}}{dR_L} = \frac{S^2(\Delta T)^2}{(R_L + R_{int})^2} - \frac{2S^2(\Delta T)^2 R_L}{(R_L + R_{int})^3} = 0. \quad (1.24)$$

Solving this for the load resistance gives $R_L = R_{int}$. We can now simplify equation (1.23) as,

$$P_{out} = \frac{S^2(\Delta T)^2 A}{4\rho L}. \quad (1.25)$$

Here the resistance has been converted to resistivity by $R = \rho L/A$, and the subscripts have been dropped.

Now we can write the relation for the optimized efficiency of the thermoelectric generator,

$$\eta = \frac{P_{out}}{\dot{Q}_h} = \left(\frac{4\rho\kappa}{S^2\Delta T} + \frac{2}{\eta_c} - 1 \right)^{-1}, \quad (1.26)$$

where $\eta_c = \Delta T/T_h$ is the Carnot efficiency. From this, one can extract the key physical parameters required to maximize the efficiency. These parameters define the figure of merit, Z , which is used to characterize TE materials. From this, we see that,

$$ZT = \frac{\sigma S^2 T}{\kappa}. \quad (1.27)$$

Mahan [2] gives an alternate equation for the maximum efficiency of a thermoelectric generator, which makes it easier to see how it depends on the material and device parameters.

$$\eta_{max} = \frac{\Delta T(\gamma - 1)}{\gamma T_h + T_c}, \quad (1.28)$$

where $\gamma = \sqrt{1 + ZT'}$, and $T' = (T_h + T_c)/2$. We see that as ZT gets very large, η_{max} approaches the Carnot limit.

We should underscore the fact that the maximum efficiency derived here is only accurate at the optimal current for each particular material. However, most TE devices are made with several different materials in each leg that must all operate at the same current, and thus generally don't function at optimal current. A more accurate maximum efficiency for such devices is considered by Snyder and Ursell [25]. They further discuss the importance of using compatible materials in a segmented device, such that all materials operate in nearly optimal conditions. However, at this point it is sufficient for us to show that the efficiency of a TE power

generation device can be improved by maximizing the figure of merit. Different ways that this can be accomplished are considered in the next section.

1.5 What Makes a “Good” Thermoelectric?

At this point it should be obvious that a “good” TE is a material with a large ZT . Figure 1.3 shows graphs of ZT for best p-type and n-type TE materials over a range of temperatures. The current state-of-the-art TE materials for refrigeration are $Bi_2Te_3/Sb_2Te_3/Bi_2Se_3$ alloys which have $ZT \approx 0.9$ at 300K [5]. The best high temperature TE materials include PbTe, which has $ZT \approx 1.2$ at 700K, and SiGe alloys, with $ZT \approx 0.6$ up to about 1000K [5]. In addition to such ‘normal’ broadband semiconductors, there are also several other promising structure types that are candidates for high temperature TE materials, including Skutterudites and Chevrel phases. Despite much effort, even for large temperatures the maximum ZT for any compound is still ~ 1 at room temperature, at atmospheric pressure and with no applied magnetic field. There have been a number of recent theoretical investigations to determine what kinds of materials properties are needed to increase the ZT of thermoelectrics. These developments are summarized in this section.

1.5.1 Optimizing the basic parameters of ZT

To maximize ZT we need a high electrical conductivity and Seebeck coefficient, and a low thermal conductivity. As a reference for the current values that need improvement, we can look at optimally doped $Bi_{0.5}Sb_{1.5}Te_3$ at 300K, with $\sigma = 900(\Omega \cdot cm)^{-1}$, $|S| = 220\mu V/K$, and $\kappa = 1.3W/(m \cdot K)$ (where $\kappa_l = 0.96W/(m \cdot K)$), which gives $ZT = 1$ [27]. In order to determine how to optimize each of these

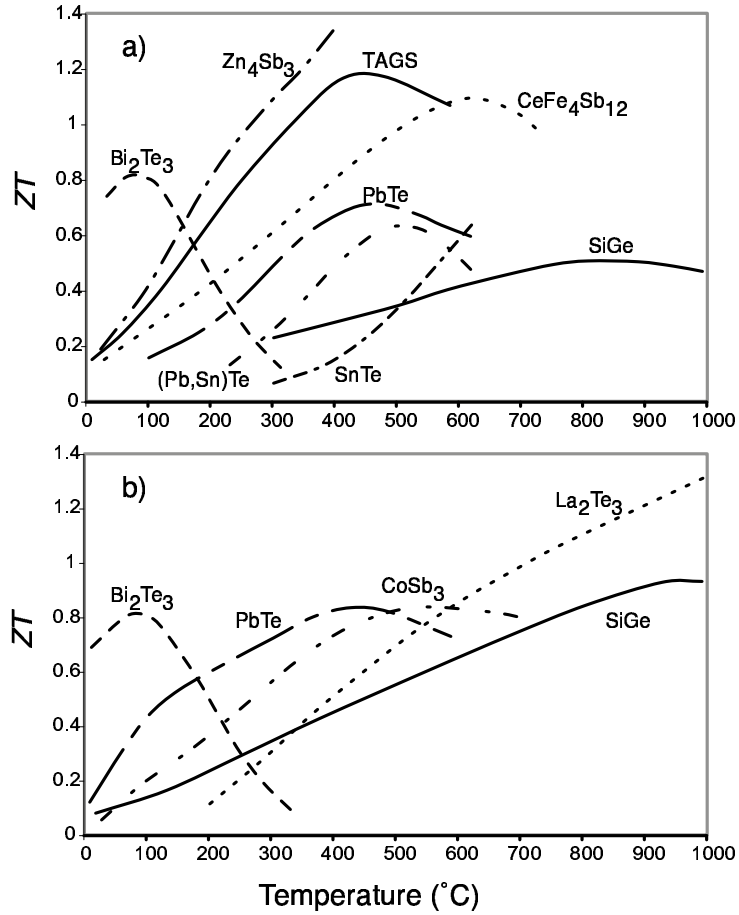


Figure 1.3: Thermoelectric figure of merit as a function of temperature (in °C) for the best (a) p-type and (b) n-type thermoelectrics. Figure adapted from [26].

values it is crucial to remember that they are not independent parameters; these are interdependent parameters that depend on each other as well as the number of charge carriers, the temperature of the material, and other materials properties. To really understand how to maximize ZT , we need to formulate a more useful relation between the main parameters.

We can begin by discussing how to optimize the density of charge carriers n , which was first discussed by Ioffe in 1957 [8]. More recent considerations can be found in Mahan [2] and Rowe [4]. By determining the dependence of σ , S , and

$1/\kappa$ on n , one can calculate how $Z = \frac{\sigma S^2}{\kappa}$ depends on the carrier density. These relations are shown schematically in Figure 1.4. It has been estimated that $Z(max)$ occurs near $n \sim 10^{19} cm^{-3}$, although the exact value of optimization depends on the material and can be anywhere from 10^{18} to 10^{21} carriers per cm^3 [8]. Thus, the best TE materials are highly-doped semiconductors, and these are the types of materials under active investigation.

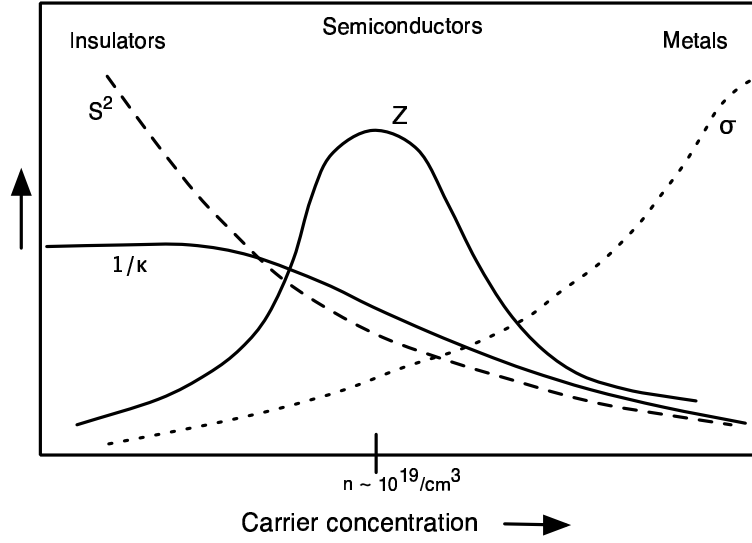


Figure 1.4: This schematic graph shows the dependence of S^2 , σ , and $1/\kappa$, and thus Z , on the charge carrier density n . Z is maximized for highly doped semiconductors with $n \sim 10^{19} cm^{-3}$. This graph is based on figures in [2, 4, 8, 12].

Next we can consider how to minimize the thermal conductivity. We first separate the thermal conductivity into its electronic and lattice (phonon) contributions,

$$\kappa = \kappa_e + \kappa_l. \quad (1.29)$$

For a metal, $\kappa_e > \kappa_l$, while for an insulator or semiconductor with a low carrier density, $\kappa_l \gg \kappa_e$. Since an optimally doped TE material is a semiconductor with a carrier concentration about 100 times smaller than the concentration of free electrons in metals, we are justified in assuming that $\kappa_l \gg \kappa_e$ [8]. To further simplify

the relation, we can apply the Wiedemann-Franz law to express the electronic part of the thermal conduction in terms of the conductivity, using $\kappa_e = \sigma L_o T$, where $L_o = 2.22 \times 10^{-8} (W \cdot \Omega / K^2)$ is the Lorentz number [4]. With these changes the FOM becomes:

$$ZT = \frac{S^2}{L_o (1 + \kappa_l / \kappa_e)}. \quad (1.30)$$

This shows that for an optimal FOM, we just need to minimize κ_l / κ_e and maximize S . It is crucial to optimize both parameters at once, since even if $\kappa_l / \kappa_e \ll 1$, we still need $S \sim 400 mV/K$ to approach a ZT of 4. However, here we will focus primarily on minimizing κ_l / κ_e , because this is easier to manage from an experimental standpoint. Furthermore, since at high temperatures the electronic thermal conductivity is of little importance [8], the main concern is minimizing the lattice thermal conductivity. Typical values of κ_l for a good TE material are $\sim 1 (W/m \cdot K)$ [2], while amorphous solids such as glasses have $\kappa_l \sim 0.1 (W/m \cdot K)$. Slack [28] was the first to recognize that a material that conducts heat like a glass and electricity like a metal would lead to great improvements in the thermoelectric figure of merit. This material is referred to as PGEC, which stands for Phonon Glass and Electron single Crystal. It has been shown that each material attains a minimum lattice thermal conductivity when all phonons have a mean free path equal to their wavelength [29].

Minimizing the lattice thermal conductivity

So the next question is, how do we actually minimize κ_l ? There are quite a number of ways to do this practically. One of the most common is to use atoms with large atomic weights, such that their movement due to lattice vibrations is minimal [1]. Another method is to synthesize materials with large unit cells, which helps

lower κ_l because heat is carried mainly by the 3 acoustical branches in a material [29]. This means that a large, complex unit cell will have many $[3(N-1)]$ optical modes that carry little heat, and only 3 modes that carry heat. Alloying also helps decrease lattice thermal conductivity by adding disorder scattering. Models relating thermal conductivity to scattering from disordered alloys show that as the disorder in the material is increased, the thermal conductivities approach those of amorphous solids [30, 31]. Unfortunately, this disorder also decreases the mobility, which should be large for a good TE material (as shown below). However, since the thermal conductivity tends to decrease faster than the mobility, alloys are overall favorable for thermoelectrics.

A new and very effective method of reducing κ_l is to create rattling structures, consisting of large atomic cages that can be intercalated with different atoms that are weakly bound and thus able to vibrate within the structure. These ‘rattlers’ were first proposed by Slack [28], and have since been discussed by others [2, 3, 5]. The most common rattling semiconductors are Skutterudites, which have the general formula MX_3 , where M is Co, Rh, or Ir, and X is P, As, or Sb [2]. Other types of rattling semiconductors are Chevrel phases, which are formulated with units of MO_6X_8 , with $X = S, Se, \text{ or } Te$. Since Chevrel phases are the focus of this research, section (1.6) is devoted to the general introduction of these materials.

Maximizing the thermopower

In addition to minimizing κ_l , we mentioned the importance of maximizing the thermopower. Since it is somewhat difficult to imagine what theoretical parameters led to the optimization of S , we will first need to look more closely at what material parameters are related to the Seebeck coefficient. Recall that the Seebeck effect is a

direct relation between the voltage generated across a material and the temperature gradient that causes it. It is simple to deduce that the charge carriers (electrons, lets say) on the hot side of the material will have higher velocity than the electrons on the cold side, due to the difference in thermal energy. This means that the electrons on the hot side are able to travel further, which leads to a net build-up of electrons on the colder end and creates a potential difference across the sample. MacDonald [14] discusses the importance of the electron velocity on the thermopower, as well as the scattering cross-section of the material (which differs from one end to the other). Furthermore, Mott and Jones [32] derive a relation between the thermopower and the electrical conductivity $\sigma(E)$, such that,

$$S \propto - \left(\frac{d \ln \sigma(E)}{dE} \right)_{E=E_F}, \quad (1.31)$$

where the subscript on the derivative means that it is evaluated at the Fermi energy E_F . Note that the equation is valid for any metal (or semimetal where $n \geq 10^{19} \text{cm}^{-3}$) at temperatures greater than the Debeye temperature (θ_D).

The conductivity can be approximated as $\sigma = \frac{ne^2\tau}{m}$ from Drude's theory of metals, where τ is the average time between collisions, and m is the effective mass of the electrons. Alternatively, Ziman [33] derives a relation between electrical conductivity, the mean free path ℓ , and the area of the Fermi surface A_{Fermi} , such that $\sigma \propto \ell \cdot A_{Fermi}$. This leads to a new description of the thermopower:

$$S \propto - \left(\frac{d \ln \ell}{dE} + \frac{d \ln A_{Fermi}}{dE} \right)_{E=E_F}. \quad (1.32)$$

Thus, the thermopower is dependent upon how ℓ and A_{Fermi} vary with energy. We note that the first term in this equation is always positive, since the mean free path of the charge carriers tends to increase with energy. Thus the second term will determine the sign of the thermopower. If the change in area of the Fermi

surface with increasing energy is negative, as it is for holes, and large enough in magnitude to overcome the first term, the thermopower will be positive. But for positive Fermi surface areas, or when the first term is dominant, the Seebeck coefficient will be negative. In practice, the second term is often larger, and thus dominates the thermopower [32, 33].

It is instructive here to discuss the simplest case of a spherical Fermi surface, in which the surface area varies with the square of the wavevector, k^2 . This relation holds for the energy of isotropic bands, such that $E = \frac{\hbar^2 k^2}{2m}$. Thus, we have the relation $A_{Fermi} \propto E$, so that $S \propto -\frac{1}{E_F}$ [22]. In degenerate semiconductors (which make the best thermoelectrics) the Fermi energy lies near a band edge, which creates a large thermopower. Indeed, the closer the Fermi energy is to the edge of the band, the higher the Seebeck coefficient will be.

1.5.2 Optimizing the materials properties

Having discussed the intrinsic characteristics of thermoelectrics that need to be optimized for a large ZT, what else do we need to consider? According to Chasmar and Stratton [34] and Mahan [2, 35], the maximum value of the figure of merit near optimal doping level can be written as a function of only 2 variables, which incorporate all of the relevant materials properties. Here we follow the definitions introduced by Mahan [2], such that $ZT = f(B, \beta E_G)$, where $\beta = 1/k_B T = 1/\tau$, and E_G is the energy gap of the semiconductor. The B factor in the figure of merit is defined for the j th band as

$$B_j = \left(\frac{k_B}{(2\pi\hbar)^2} \right) \frac{N_j \mu_j m_j^{3/2} \tau^{5/2}}{\kappa_l}, \quad (1.33)$$

such that it contains all the materials properties of the TE. We write N_j as the degeneracy of the band, including spin degeneracy, while μ_j is the mobility, and m_j

is the effective mass which for non-isotropic media becomes $m_j^{3/2} = \sqrt{m_{jx}m_{jy}m_{jz}}$. The Boltzmann constant k_B is equal to $1.381 \times 10^{23} (J/K)$ and $\hbar = 1.055 \times 10^{-34} (J \cdot s)$ is the Plank constant divided by 2π .

We can also define a quality factor (Q_j) for each band such that,

$$Q_j = N_j \mu_j \left(\frac{m_j}{m_e} \right)^{3/2}, \quad (1.34)$$

which has units of mobility, ($cm^2/(V \cdot s)$). This factor includes all the parameters in the B factor that are properties of the charge carrier. Using this, we can rewrite the B factor as,

$$B = C_B \frac{Q_j}{\kappa_l} \left(\frac{T}{300} \right)^{5/2}, \quad (1.35)$$

with constant $C_B = 4.55 (V \cdot J/K \cdot m^3)$. It is useful to write B in this form because it illuminates the material properties that need to be optimized for a good thermoelectric, which include Q_j , κ_l , and T .

Maximizing the band parameters

We will first consider ways to maximize the quality factor while keeping βE_G constant. This effectively keeps T constant as well, since the optimal temperature is basically determined by the energy gap (as discussed later). Additionally, since we have already discussed how to minimize κ_l in section 1.5.1, we need not consider it further. Thus we are left with optimizing Q_j , which involves maximizing N_j , μ_j , and m_j . We begin by discussing the importance of the band degeneracy in maximizing the FOM, since it is directly proportional to the quality factor and can cause significant changes in the efficiency of the TE. According to Mahan [2], there must be at least 4 equivalent band minima for a good TE, which gives a band degeneracy N_j of 8 (including spin degeneracy), whereas a single band minima

would only give $N_j = 2$. Unfortunately, there have been very few experimental investigations about how to actually increase the degeneracy.

Next we will consider the effective mass. A glance at equation (1.34) implies that the effective mass has the largest impact on the quality factor. However, since the mobility depends on the effective mass as $\mu_j = \frac{e\tau}{m_j}$, the quality factor does not have as high a dependence on m_j as it may initially seem. Nevertheless, it is still a critical materials parameter, and it is important to have the largest possible effective mass. It has been shown that to maximize the effective mass the semiconductor should have an indirect band gap, which means the valence band maxima and the conduction band minima occur at different points in k-space. For a direct band gap semiconductor, it can be shown that $m_j \sim E_G$ [36], which gives small effective masses for semiconductors.

Despite the fact that a smaller effective mass gives a higher mobility, it is better to have a large effective mass from an indirect band gap and to try to increase the mobility in other ways. For example, minimizing electronegativity differences between the atoms in a TE material will help to increase the mobility. Electronegativity describes an atom's tendency to take an electron away from or donate an electron to another atom. Each element has a distinct value of electronegativity. A small electronegativity difference between atoms in a compound implies mostly covalent bonding. This is favorable in TE materials because the mobility is not reduced through polar scattering by phonons. (Refer to Pauling [37] for more information about electronegativity from a chemistry standpoint, and Mahan [2] or Slack [28] for its relation to thermoelectrics.)

Another property which favorably affects mobility is a large dielectric constant, which leads to a strong screening of impurities. Elements with a high atomic num-

ber or a high polarizability are known to have large dielectric constants. This makes Se, Te, and Sb doubly good as material components in thermoelectric compounds, as they have both, and explains why there is usually at least one of these elements in the best TE materials [2].

Optimizing the band gap

Next we can consider how to optimize ZT in terms of the energy gap, which can be found by setting B constant and varying βE_G . Mahan [2] determined that a good TE material would have small E_G , such that $E_G \sim nk_B T$, where $6 \leq n \leq 10$ and T is the best temperature for optimal ZT for that material [38]. These energy gaps are generally large enough to prevent the combination of electron and hole contributions to the TE effects, which limits the materials efficiency. Although even larger band gaps would also limit this type of activity, materials with $E_G > 10k_B T$ are not optimized for use in TE devices. Furthermore, the band gap follows this “ $10k_B T$ ” rule for $T \geq 300K$, but for lower temperatures or when E_G is reduced through alloying, this rule is no longer valid [2].

Theoretical limits on maximum ZT

There have been various theoretical searches to find a maximum possible ZT, based on a wide range of fields. Littman and Davidson [39] argue that from an irreversible thermodynamics standpoint there is no finite limit on the FOM. However, Rittner and Neumark [40] claim that thermodynamics is not appropriate for these calculations, and instead use statistical and kinetic methods with a specific physical model of a solid to calculate the limit. This model is based on the two-band semiconductor model published by Simon [41]. Ritter and Neumark report that there

is a finite limit to ZT , but, since the value depends on the model used for the calculations, were unable to find a unique $(ZT)_{max}$. Mahan [35], who made efforts to limit his modeling and calculations to realistic values of the physical parameters, found $(ZT)_{max} \sim 2$. If accurate, this clearly restricts the possibilities of finding a “good” TE, although it still leaves hope of improvement upon current thermoelectric materials. However, Mahan and Sofo [42] have recently done calculations for the maximum FOM from optimization of the electronic structure and found a $(ZT)_{max} \sim 14$ using reasonable physical parameters but with an unphysical delta function for the transport distribution.

Based on all of these reports, it seems that there is no known distinct limit on the thermoelectric figure of merit, as each calculation is limited by the approximations of the model. However, we are at least able to see some promise of finding improved materials, encouraging the experimental search to continue.

Summary of requirements for a good TE

This concludes the discussion of the properties requirements for good thermoelectrics. Since a wide range of properties have been considered in the section, we will end with a summary of the most important points. For a high figure of merit, a thermoelectric needs to have as many of the following properties as possible:

1. minimal lattice thermal conductivity κ_l , which can be accomplished by using complex structure types made from atoms with high atomic weights, alloys, and rattling atomic cages;
2. maximal thermopower S , which occurs when the Fermi level is very near the edge of the valence or conduction band (for highly degenerate semiconduc-

tors);

3. maximal quality factor Q_j , which includes having a large band degeneracy N_j of at least 8 (including spin degeneracy), a large effective mass m_j which implies an indirect band gap, and a high mobility μ_j from small electronegativity differences and large polarizabilities; and
4. an energy gap $\sim 10k_B T$ for temperatures above 300K.

Keeping all these properties in mind, we can next look at Chevrel phases to determine why they should be good thermoelectrics. These materials are introduced in the following section.

1.6 Chevrel Phases

The research reported in this thesis involves the synthesis and study of Chevrel phase materials, chosen for their potential as good high temperature thermoelectrics. The Chevrel phase (or ternary molybdenum chalcogenide) structure was first discovered in 1971 by R. Chevrel [43] and was extensively studied in subsequent years because several of these materials are superconductors with high critical magnetic fields and modest critical temperatures ($\sim 16K$). As a result, there have been many experimental and theoretical investigations of these materials. Reviews such as references [44] and [45] summarize much of this research.

So why are Chevrel phases interesting from a thermoelectric standpoint? We have already emphasized the importance of having a low lattice thermal conductivity. Chevrel phases are one of the ‘rattling’ semiconductors, with units that consist of an atomic cage that can be intercalated with various atoms and act as a deflection center for phonons. These type of structures are extremely effective

at minimizing κ_l . The Chevrel phase structure is additionally good for lowering lattice thermal conductivity because they assume complex structures which incorporate many atoms (14 or more per unit cell), with relatively heavy atomic weights. These aspects make Chevrel phases likely candidates to reach the lower limit of κ_l , thus making them encouraging prospects for improved high temperature TE materials [46].

The Chevrel structure

Chevrel phases are generally described by the chemical formula $M_xM_o_6X_8$, with M = metal (usually), and X = chalcogen (normally S, Se, or Te). This discussion will focus on Chevrel structures using Se as the chalcogen, since it was used in all of the Chevrel phases synthesized and studied here. It has been suggested that selenides are preferable from a TE standpoint, since Se has a higher atomic mass (which lowers κ_l) and tends to be more covalent in bonding (which increases μ) [47]. The basic Chevrel unit is the Mo_6Se_8 cluster, known in molecular chemistry as the $(Mo_6Cl_8)^{4+}$ cluster [48].

Before we discuss the structure and packing of the Chevrel phase units, it is useful to mention that the M atoms are intercalated into different cavities depending on their size. There are three different cavity types formed by the packing of the Mo_6Se_8 units, and while large M atoms like Pb and Sn can only fit in the largest cavity, smaller atoms like Cu, Fe, and Ni can also fit into one of the two smaller cavities.

We will now briefly describe the Chevrel framework, generally following Hughbanks and Hoffmann [49]. It is easiest to start with one unit cell of $PbMo_6Se_8$ as in Figure 1.5, keeping in mind that the structure of Mo_6Se_8 is basically the same with-

out the Pb (and also noting that Pb could be replaced by any other large metal atom to give a similar structure). The Mo_6Se_8 structure consists of a slightly distorted inner octahedra of Mo atoms (with bond lengths $Mo - Mo \simeq 2.7\text{\AA}$) surrounded by a cube of Se atoms ($Mo - Se \simeq 2.6\text{\AA}$). The Mo atoms are positioned such that they lie above the center of the cube faces. Another way to picture this is such that the chalcogen atoms are positioned to cap each of the triangular faces of the octahedra.

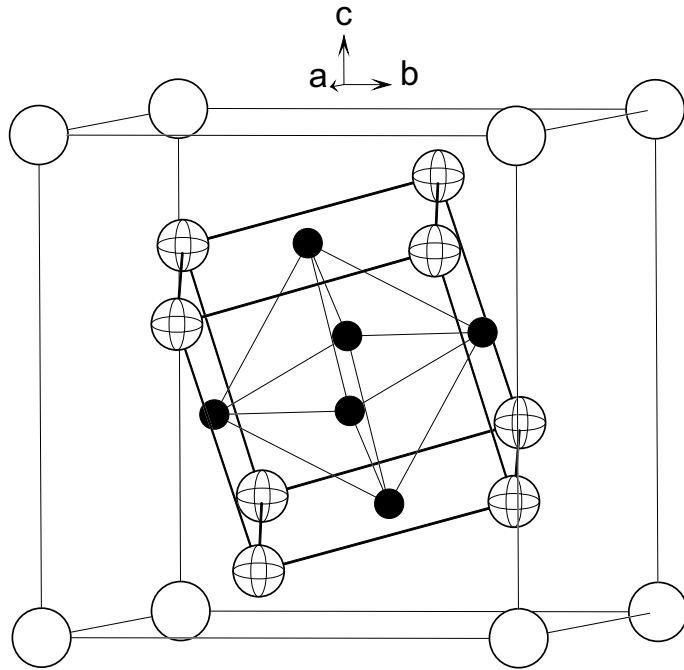


Figure 1.5: $PbMo_6Se_8$ Chevrel phase unit. Notice that the unit cell is almost cubic and consists of an octahedra of Mo atoms (black) inside a cube of Se atoms (crossed), rotated within a cubic Pb (white) structure.

The Pb atoms pack in a simple cubic lattice, with a lattice constant $\sim 6.54\text{\AA}$. We can construct the full Chevrel framework by mentally placing the Mo_6Se_8 cluster inside the simple cubic Pb lattice, while retaining the cubic symmetry. The final step is to rigidly rotate the Mo_6Se_8 structure by $\sim 26^\circ$ around the 3-fold body axis. This completed structure is shown in Figure 1.5. It has been suggested

that the reason the Mo_6Se_8 units rotate is to minimize the intercluster chalcogen-chalcogen repulsions, as it allows the Mo atom of one cluster to interact directly with a chalcogen from the next cluster [48, 49]. Note, however, that this rotation breaks the cubic symmetry, so the Chevrel structure is rhombohedral - generally ($R\bar{3}$) with a rhombohedral angle $\sim 89^\circ$, although intercalation of different M atoms tends to distort the structure to lower symmetry. For more structural details of the basic Chevrel unit, see references [44, 48, 49, 50, 51].

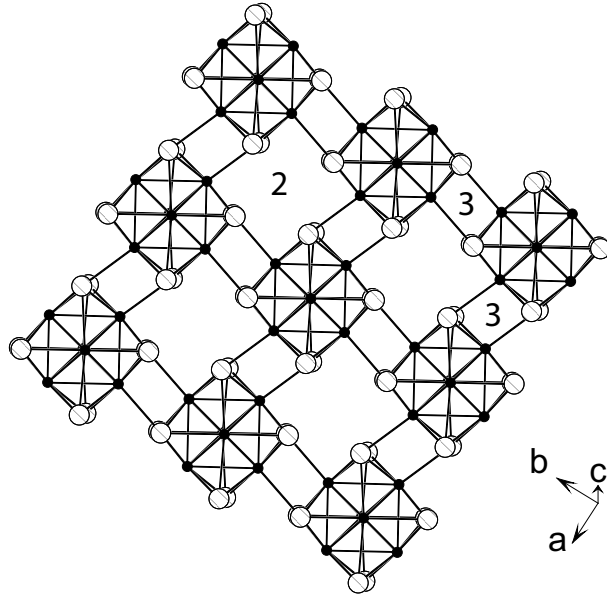


Figure 1.6: Extended structure of Chevrel phase Mo_6Se_8 unit showing two of the channels formed by packing. The Mo atoms are black, and the Se atoms are white with cross-hatching.

Figure 1.6 shows the packing of the Chevrel Mo_6Se_8 units, and displays two of the smaller cavities. The cavity labeled (2) is large enough for some small intercalated metal atoms, but cavity (3) is not. The largest cavity consists of an almost cubic channel made by the Chevrel units, and is shown in Figure 1.7. A large metal atom in this cavity will bond with Se atoms from 8 separate Chevrel clusters. Figure 1.8 shows all the cavities, and their relation to the Chevrel units.

For further description of these cavities, refer to Chevrel and Sergent [50] or Roche [51].

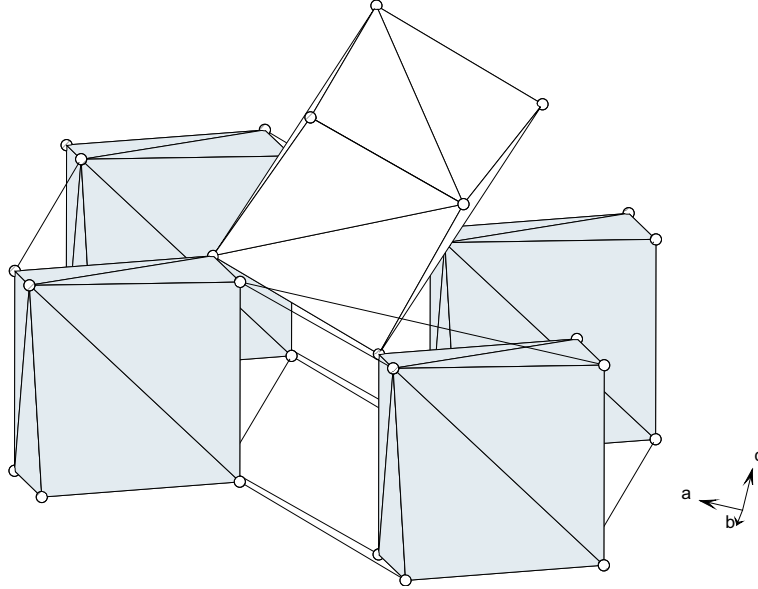


Figure 1.7: Large cavity formed by packing of Chevrel clusters is shown here as a white polyhedra. The Mo_6Se_8 units are displayed as grey polyhedra.

Large atoms can only be intercalated into the largest cavity, and give a stoichiometric filling with $x \approx 1$ (in terms of the chemical formula $M_xMo_6X_8$) [46, 51]. Smaller atoms like Ni, Cu, and Ti that fit into the one of the other cavities, and are statistically distributed around several different sites within the unit cell. The theoretical filling fraction for these atoms is $x = 6$, although it has been found experimentally that maximum filling occurs at $x = 4$ [52]. It turns out this filling limit is due to electronic factors, not geometric factors as previously speculated [51].

The addition of M atoms to the structure is used to increase the number of valence electrons on the Mo octahedra. As the number of valence electrons increases, the Mo octahedra contracts and becomes less distorted [53]. In the pure Mo_6Se_8 unit, the molybdenum cluster has 20 valence electrons, calculated as fol-

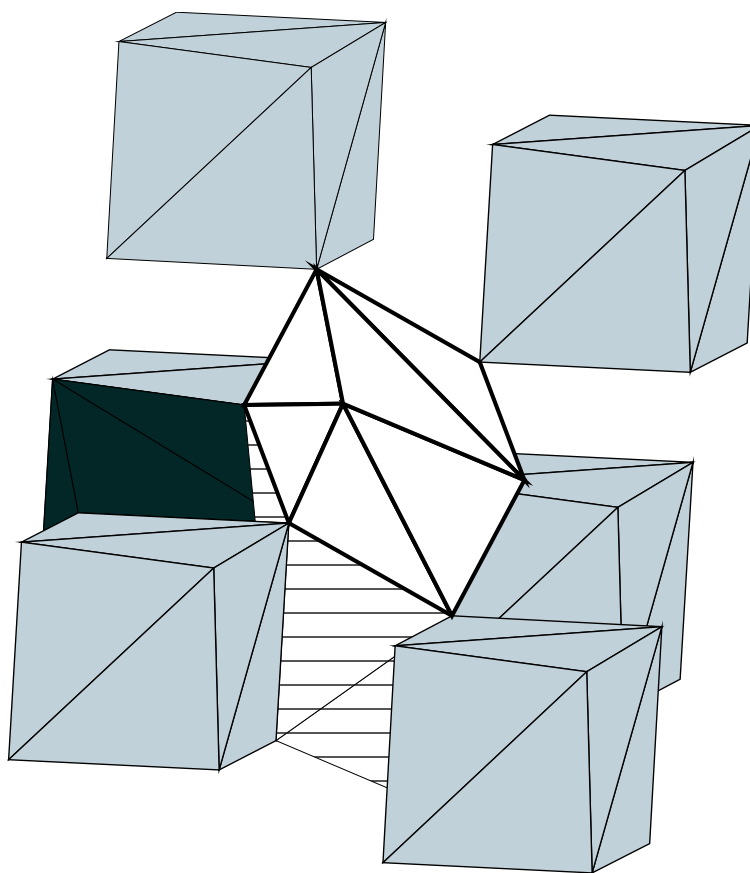


Figure 1.8: All cavities formed by packing of Chevrel clusters are displayed here. The largest cavity is shown as a white polyhedra, cavity 2 which holds the smaller intercalated atoms is cross-hatched, and cavity 3 is grey.

lows; the Mo atoms contribute $6 \times 6 = 36$ electrons, while the Se atoms (in the -2 oxidation state) take away $2 \times 8 = 16$ electrons. Intercalated atoms are chosen such that they contribute a particular number of extra electrons to the Chevrel unit. When there are 24 valence electrons, the octahedra should become regular, and the compound becomes semiconducting (see band structure calculations below). This corresponds to 4 extra valence electrons for each Mo, a number which is sometimes referred to as a “cluster-valence-electron-concentration,” or cluster-VEC [53]. Usually, Chevrel phase materials have a cluster-VEC between 3.3 and 4 [46].

DOS and Band Structure; Mo_6Se_8

Changing the cluster-VEC is equivalent to changing the Fermi level in the conduction band [53]. Since intercalation of M atoms affects the electrical and thermal properties of the Chevrel phases, it presents a method of tuning the properties to maximize the FOM. Band structure calculations can be done to determine theoretically whether a particular Chevrel phase compound will be a semiconductor. Nunes and Mazin [54] show the calculated band structure of Mo_6Se_8 , which is metallic. We have also calculated the density of states (DOS) and band structure using the extended Hückel method using the YAeHMOP software¹ and known positions of the atoms [55]. These are shown in Figures 1.9 and 1.10. Since the approximations and modeling of each program is different, small changes are expected when comparing the results, but the important features of the bands and the DOS should still be apparent and consistent.

There are a total of 68 electrons in the p and d states of Mo_6Se_8 , which makes the Fermi level 4 electrons short of an energy gap. This gap has been shown by Hughbanks and Hoffman [49] to be $\sim .8eV$ wide, which is similar to our calculated gap shown in Figure 1.9. (Since $10k_B T$ at 1000K is $.86eV$, Chevrel phases have ideal band gaps for high temperature thermoelectrics). The addition of 4 electrons should make the structure semiconducting, which is shown by the new position of the Fermi level, just above the highest filled band. (The small Gaussian tail above the Fermi level which makes this compound appear metallic is due to the YAeHMOP calculation software, which uses a broadening function to avoid infinities in the DOS that could arise from one-dimensional bands.) Notice

¹The YAeHMOP calculations were done using 1000 \vec{k} points, with bin spacing of 0.05. The results of the DOS calculations were then smoothed using Gaussian functions with a broadening of 250.

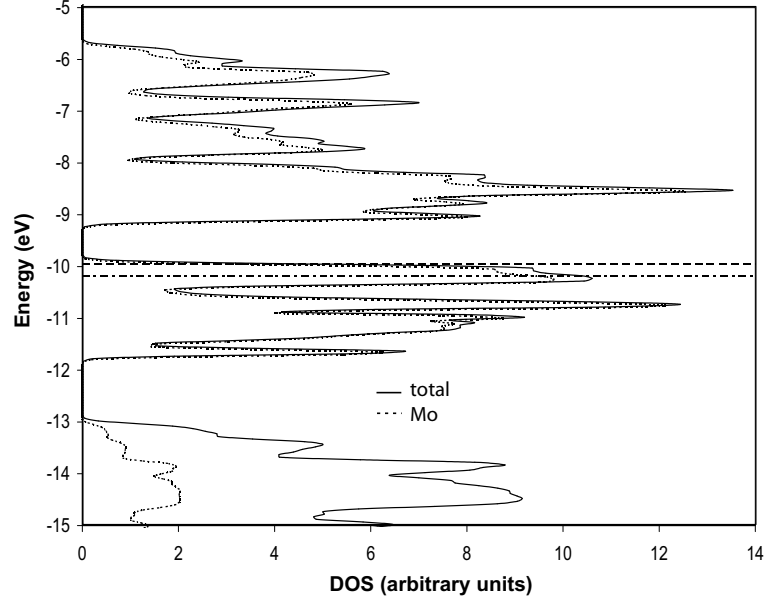


Figure 1.9: Calculated DOS for Mo_6Se_8 from YAeHMOP. The dash-dotted line at -10.18 eV shows Fermi energy for neutral Mo_6Se_8 , and the dashed line at -9.94 eV shows the Fermi energy for Mo_6Se_8 plus 4 extra electrons.

that most of the contribution to the DOS near E_F is due to the Mo orbitals, as can be seen from the projected DOS.

Band structure calculations have been reported for a number of different $M_xMo_6X_8$ Chevrel structures (see, for example [49, 56, 57, 58, 59]). Our calculated band structure of Mo_6sSe_8 is presented in Figure 1.10. The Fermi level (shown with a dashed line) is 2 bands below the band gap. This further demonstrates that 4 more electrons are needed to make this compound semiconducting, with a Fermi level just above the highest filled band.

Intercalation and substitution

Adding 4 electrons to the structure can be done by intercalation of an M atom, substitution of some of the Mo atoms, or both. However, substitutional impurities at the Mo site (i.e. $Mo \rightarrow Ru, Re$) tend to strongly scatter conduction electrons,

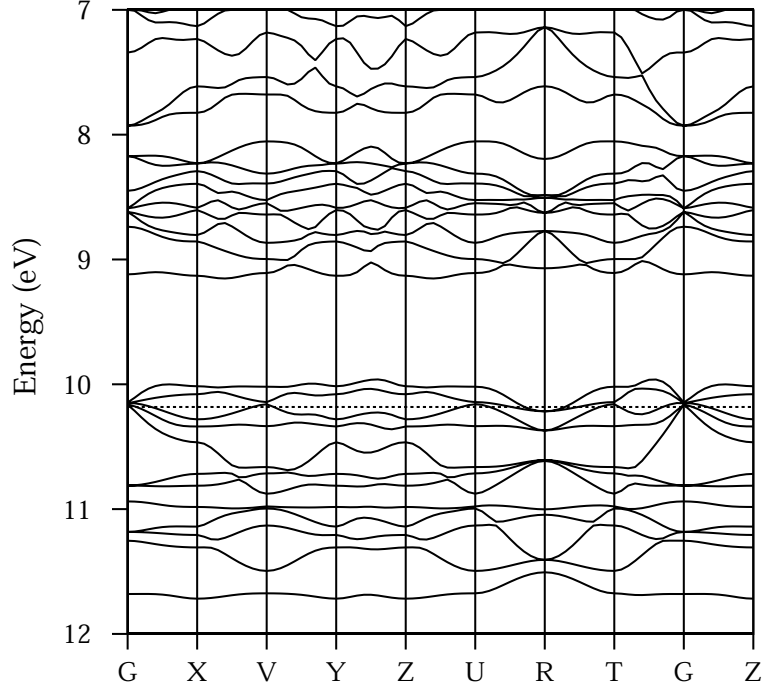


Figure 1.10: Band structure of Mo_6Se_8 electrons calculated from YAEHMOP. The x-axis shows the usual special \vec{k} points of high symmetry. The Fermi level is shown with a dashed line, located at -10.182 eV.

which limits the carrier mobility. Since the valence states are mostly due to Mo-Mo bonding, small changes in the geometric structure from intercalation can cause large changes in the band structure. This implies a strong electron-phonon interaction, limiting the mobility at high temperatures. When the electronic structure of $M_xMo_6X_8$ is similar to that of Mo_6X_8 , a reasonable value for μ is expected [54].

The large flexibility of choices for intercalation and substitution atoms make Chevrel phases promising candidates for thermoelectrics, with a distinct ability to tune their electronic and structural properties. The most appealing characteristic of Chevrel phases is the minimal lattice thermal conductivity that is a result of the complex rattling structure with rather high atomic weight elements. It is reasonable to suppose Chevrel phases can also be designed to incorporate some

of the other properties necessary for good thermoelectrics, which was the main goal of this research. The following chapters will discuss the results of these efforts.

REFERENCES

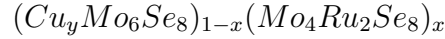
- [1] F. J. DiSalvo, *Science* **285**, 703 (1999).
- [2] G. D. Mahan, *Solid State Phys.*, volume 51, chapter Good Thermoelectrics, pages 82-157, Academic Press, New York (1998).
- [3] B. Sales, *Mater. Res. Soc. Bull.* **23**, 15 (1998).
- [4] D. M. Rowe, editor, *CRC Handbook of Thermoelectrics*, CRC Press, Boca Raton, Fl. (1995).
- [5] G. D. Mahan, B. Sales, J. Sharp, *Phys. Today* **50**, 42 (1997).
- [6] T. J. Seebeck, *Abhandlungen der Deutschen Akademie der Wissenschaften zu Berlin*, 265 (1822-1823).
- [7] J. C. Peltier, *Ann. Chim.* **56**, 371 (1834).
- [8] A. F. Ioffe, *Semiconductor Thermoelements and Thermoelectric Cooling*, Infosearch Ltd., London (1957).
- [9] W. Thomson (Lord Kelvin), *Proc. Roy. Soc. Edinburgh, Vol. III*, Neil and Company, Edinburgh (1851), pp. 91.
- [10] L. Onsager, *Phys. Rev.* **37**, 405 (1931).
- [11] L. Onsager, *Phys. Rev.* **38**, 2265 (1931).
- [12] R. R. Heikes and R. W. Ure, *Thermoelectricity: Science and Engineering*, Interscience, New York (1961).
- [13] M. W. Zemansky, *Heat and Thermodynamics, 2nd ed.*, McGraw-Hill, New York (1937).
- [14] D. K. C. MacDonald, *Thermoelectricity: an Introduction to the Principles*, Wiley, New York (1962).
- [15] C. Wood, *Rep. Prog. Phys.* **51**, 459 (1988).
- [16] W. Thomson (Lord Kelvin), *Proc. Roy. Soc. Edinburgh, Trans.* **21**, Part I, 123 (1857).
- [17] H. B. Callen, *Phys. Rev.* **73**, 1349 (1948).
- [18] S. R. de Groot, *Thermodynamics of Irreversible Processes*, Interscience, New York (1951).
- [19] P. J. Price, *Phys. Rev.* **104**, 1223 (1956).

- [20] C. A. Domenicali, *Rev. Mod. Phys.* **26**, 237 (1954).
- [21] M. H. Cobble, *CRC Handbook of Thermoelectrics*, chapter 39: Calculations of Generator Performance, pages 489-501, CRC Press, Inc., Boca Raton, FL, 1995.
- [22] K. Poduska, *A materials approach to improving the efficiency of thermoelectric cooling devices*, PhD thesis, Cornell University, 2001.
- [23] G. D. Mahan, *J. Appl. Phys.* **70**, 4551 (1991).
- [24] C. A. Domenicali, *J. Appl. Phys.* **25**, 1310 (1954).
- [25] G. J. Snyder, T.S. Ursell, *Phys. Rev. Lett.* **91**, 148301 (2003).
- [26] G. J. Snyder, *The Science and Materials behind Thermoelectrics*, <http://www.its.caltech.edu/~jsnyder/thermoelectrics/science_page.htm>, (7/14/2005).
- [27] W. M. Yim, F. D. Rosi, *Solid State Electron.* **15**, 1121 (1972).
- [28] G. A. Slack, *CRC Handbook of Thermoelectrics*, chapter 34: New materials and performance limits for thermoelectric cooling, pages 407-440, CRC Press, Inc., Boca Raton, FL, 1995.
- [29] G. A. Slack, *Solid State Physics*, volume 34, chapter The Thermal Conductivity of Nonmetallic Crystals, pages 1-71, Academic Press, Inc., New York (1979).
- [30] B. Abeles, *Phys. Rev.* **131**, 1906 (1963).
- [31] D. G. Cahill, S. K. Watson, R. O. Pohl, *Phys. Rev. B* **46**, 6131 (1992).
- [32] N. F. Mott and H. Jones, *The Theory of the Properties of Metals and Alloys*, Dover Publications, New York, 1936.
- [33] J. M. Ziman, *Electrons and Phonons*, Oxford University Press, London, 1960.
- [34] R. Chasmar, R. Stratton, *J. Electron. Control* **7**, 52 (1959).
- [35] G. D. Mahan, *J. Appl. Phys.* **65**, 1578 (1989).
- [36] W. A. Harrison, *Solid State Theory*, McGraw-Hill Book Co., New York (1970).
- [37] L. Pauling, *The Nature of the Chemical Bond, 2nd ed.*, Cornell University Press, Ithaca (1939).
- [38] J. O. Sofo, G. D. Mahan, *Phys. Rev. B* **49**, 4565 (1994).

- [39] H. Littman, B. Davidson, *J. Appl. Phys.* **32**, 217 (1961).
- [40] E. S. Ritner, G. F. Neumark, *J. Appl. Phys.* **34**, 2071 (1963).
- [41] R. Simon, *J. Appl. Phys.* **33**, 1830 (1962).
- [42] G. D. Mahan, J. O. Sofo, *Proc. Natl. Acad. Sci.* **93**, 7436 (1996).
- [43] R. Chevrel, M. Sergent, J. Prigent, *J. Solid State Chem.* **3**, 315 (1971).
- [44] O. Fischer, *Appl. Phys.* **16**, 1 (1978).
- [45] O. Fischer, M. B. Maple, ed., *Topics in Current Physics; Superconductivity in Ternary Compounds I*, chapter Chemistry and Structure of Ternary Molybdenum Chalcogenides, pages 25-86, Springer-Verlag, Berlin (1982).
- [46] T. Caillat, J.-P. Fleurial, G. J. Snyder, *Solid State Sci.* **1**, 535 (1999).
- [47] K. Yvon, *Curr. Top. Mat. Sci.* **3**, 53 (1979).
- [48] J. K. Burdett, J.-H. Lin, *Inorg. Chem.* **21**, 5 (1982).
- [49] T. Hughbanks, R. Hoffmann, *J. Am. Chem. Soc.* **105**, 1150 (1983).
- [50] R. Chevrel, M. Sergent, *Topics in Current Physics, Superconductivity in Ternary Compounds I*, Springer-Verlag, Berlin, 25 (1982), ed. O. Fisher and M. B. Maple.
- [51] C. Roche *et al.*, *J. Phys.: Condens. Matter* **10**, L333 (1998).
- [52] T. Callat, J.-P. Fleurial, *J. Phys. Chem. Solids* **59**, 1139 (1998).
- [53] K. Yvon, A. Paoli, *Solid State Commun.* **24**, 41 (1977).
- [54] R. W. Nunes, I. I. Mazin, *Phys. Rev. B.* **59**, 7969 (1999).
- [55] O. Bars, J. Guillevic, D. Grandjean, *J. Solid State Chem.* **6**, 48 (1973).
- [56] D. W. Bullett, *Phys. Rev. Lett.* **39**, 664 (1977).
- [57] C. Roche *et al.*, *Phys. Rev. B* **60**, 16442 (1999).
- [58] L. F. Mattheiss, C. Y. Fong, *Phys. Rev. B* **15**, 1760 (1977).
- [59] O. K. Andersen, W. Klose, H. Nohl, *Phys. Rev. B.* **17**, 1209 (1978).
- [60] N. W. Ashcroft, N. D. Mermin, *Solid State Physics*, Harcourt College Publishers, Fort Worth (1976).
- [61] F. J. Blatt, P. A. Schroeder, C. L. Foiles, D. Greig, *Thermoelectric Power of Metals*, Plenum Press, New York (1976).

CHAPTER 2

SYNTHESIS AND THERMOELECTRIC PROPERTIES OF



In this Chapter, we discuss the Chevrel phase solid solutions $(Cu_yMo_6Se_8)_{1-x}(Mo_4Ru_2Se_8)_x$, with $y = 2, 4$ and $x \approx 0, 0.2, 0.4, 0.6, 0.8$, and 1. The resistivity and Seebeck coefficient are reported from room temperature up to approximately 1100K. From these measurements we estimate the thermoelectric figure of merit ZT , and the highest is $ZT \sim 0.3$ at 1000K. The high temperature transport properties of the semiconducting Chevrel phase $Mo_4Ru_2Se_8$ are reported here as well. Before describing the experimental details, we will first review and motivate this investigation.

2.1 Motivation and review

As discussed in detail in Chapter 1, to optimize ZT we need σ and S to be maximized, and κ to be minimized. Most TE research focuses on synthesizing doped semiconductors with very low thermal conductivity. It has been shown that the best TE materials are semiconductors with $n \sim 10^{19}cm^{-3}$ [1]. Slack [2] proposed a material that could minimize lattice thermal conductivity would consist of a loosely bound atom inside a cage-like structure of atoms. If such a material could also be made to conduct electricity like a metal, it would be ideal for thermoelectrics. Chevrel phase materials, first discovered by R. Chevrel in 1971 [3], exhibit this ‘rattling’ structure type. Previous studies of these types of materials for TE applications show promising results [4]. An additional consideration for improving the efficiency of cascaded power generation devices is using materials with similar compatibility factors, as discussed by Snyder and Ursell [5]. Although

SiGe has a significantly lower compatibility factor than other materials used in such devices, we believe Chevrel phase materials may have smaller compatibility differences.

Chevrel phase materials, based on the Mo_6X_8 structure, have empty cavities throughout the cluster network. Two of these cavities are large enough to provide intercalation sites for a wide range of atoms. The intercalation of various atoms can be used to tune the electrical and thermal properties of Chevrel phase compounds, which is extremely beneficial from a thermoelectric standpoint. Band structure calculations show that Mo_6Se_8 needs 4 additional electrons to fill the partially occupied band and become semiconducting [6]. These intercalation sites provide an easy way to add electrons to the structure. Additionally, substitution of either *Ru* or *Re* for *Mo* provides another way to add electrons to the system without significantly changing the cluster size or shape. However, it is often difficult to add 4 electrons to the Chevrel cluster, and filled compounds often have between 3.3 – 4 electrons per cluster [4].

$Cu_{3.1}Mo_6Se_8$ is one of the best high temperature Chevrel phase TE materials to date [4], with a reasonably large power factor and a low thermal conductivity. It has a $ZT \sim 0.4$ at around 1000K, and would likely have a significantly larger figure of merit if it was made semiconducting. However, so far efforts to increase the filling of Cu have not been successful.

Here we study a combination of intercalation and substitution into the Chevrel network by alloying the intercalated compound $Cu_yMo_6Se_8$ with the substituted compound $Mo_4Ru_2Se_8$. By using a combination of methods to add electrons to the cluster, we hope to be more successful in synthesizing a semiconducting Chevrel phase with 4 extra valence electrons per cluster. We further expect that

alloying will help decrease the lattice thermal conductivity of the material, by adding disorder to the structure.

2.2 Experimental

2.2.1 Reagents

Since the samples are sensitive to oxygen during initial reaction synthesis, efforts were made to minimize oxygen present in the system. The following reagents were reduced in forming gas before use: *Cu* (Fisher Scientific Co., electrolytic powder), *Mo* (Aldrich, 99.9% purity, -100 mesh), and *Ru* (Cerac, 99.95% purity, -325 mesh). A flow-through furnace was used to heat the powders during reduction. The *Cu* powder was heated from room temperature to 300°C over 1 hour, held there for 3 hours, and allowed to cool back to room temperature naturally with the furnace turned off. The *Mo* and *Ru* powders were heated to 1000°C over 5 hours, held at that temperature for 30 hours, and then cooled naturally. After reduction these powders were transferred to an argon-filled glove box and weighed without exposure to air. *Se* (99.9% purity, 4mm pellets) was used as received.

2.2.2 Sample preparation

The $(\text{Cu}_y\text{Mo}_6\text{Se}_8)_{1-x}(\text{Mo}_4\text{Ru}_2\text{Se}_8)_x$ samples were synthesized by annealing mixtures of previously synthesized $\text{Cu}_2\text{Mo}_6\text{Se}_8$ or “ $\text{Cu}_4\text{Mo}_6\text{Se}_8$ ” with $\text{Mo}_4\text{Ru}_2\text{Se}_8$. For each series, alloys were synthesized for $x \approx 0.2, 0.4, 0.6,$ and 0.8 . These mixtures were ground in an agate mortar, and each sample was pressed into a pellet and sealed in an evacuated quartz ampoule. The Cu_2 alloys were then annealed at 1100°C for 4 days, and the Cu_4 alloys were annealed at 1100°C for 3 days

twice, with intermittent grinding. The only significant impurity in any sample was $MoSe_2$, although several of the alloys formed copper selenide on the pellet surfaces during the final annealing process. This Cu_2Se was removed from the surface before sample characterization.

The starting materials $Cu_2Mo_6Se_8$, “ $Cu_4Mo_6Se_8$ ”, and $Mo_4Ru_2Se_8$ were each synthesized by mixing stoichiometric amounts of the elements and sealing them in evacuated quartz ampoules. The elements were then reacted by heating these ampoules to $400^\circ C$ over 1 day, holding them there for 1 day, and letting them cool naturally. After this initial reaction, each sample was mixed well by shaking the unopened ampoule, and then heated again to $1100^\circ C$ over 1 day, held there for 2 days, and cooled naturally. Both of the copper-containing compounds were single-phase after this reaction, and were not annealed again. The $Mo_4Ru_2Se_8$ sample was mechanically ground in an agate mortar and pestle and pressed into a pellet in a hardened steel and tungsten carbide die. The pellet was vacuum-sealed in another quartz ampoule, heated to $1200^\circ C$ over 1 day, and then annealed for 3 days. This high-temperature annealing was performed twice to get a sufficiently pure specimen. Powder X-ray diffraction was used to establish phase purity of the pattern.

2.2.3 Powder X-Ray diffraction analysis

After synthesis, the samples were characterized using powder X-ray diffraction (XRD). The data was collected with a Scintag 2000 theta-theta diffractometer, using $Cu K\alpha$ radiation ($\lambda = 1.54059\text{\AA}$, 45kV, 40mA). Each sample was ground finely with a mortar and pestle before the scan. XRD scans were taken after each anneal, with 2θ from $10 - 70^\circ$. These scans were taken with a step size of 0.02°

and a rate of 2 deg/min. The annealing process was completed when the sample contained only one set of Chevrel phase peaks and minimal impurities. In general, the only impurity perceived with powder XRD was $MoSe_2$, which made up less than 5% of each sample.

The powder XRD scans of the finished samples were used to calculate unit cell parameters with the program TREOR [7]. More than 25 Bragg peaks were used to index each sample.

2.2.4 Transport property measurements¹

In order to get dense samples, the finely ground polycrystalline powders were hot-pressed in high-density graphite dies (POCO). The hot-pressing was conducted at a pressure of about 20000 psi and at 1223K for 1.5 hours under argon atmosphere. Cylindrical pellets obtained by this method were about 12mm in diameter. The geometrical densities were calculated from the measured dimension and weight of each sample, and found to be at least 95% of the theoretical density.

Samples in the form of discs (typically about 1mm thick) were cut from each cylinder using a diamond saw. These discs were used for electrical and thermal transport properties. The Seebeck coefficient measurement was performed on the remaining cylinder. All these physical properties were measured from room temperature to about 1200K.

The electrical resistivity, ρ , was measured using the van der Pauw technique with a current of 100mA using a special high-temperature apparatus [8]. The Seebeck coefficient, S , was measured using a high temperature light pulse technique

¹These measurements were performed by Franck Gascoin at Jet Propulsion Laboratories (JPL). These experimental details were also provided by F. Gascoin.

[9].

2.2.5 Microprobe analysis

The elemental composition of the samples was determined by high-precision microprobe analysis using a JEOL 8900 electron microprobe and pure metal standards. To prepare the samples for this analysis, a small piece of the hot-pressed pellet of each compound was fixed at the end of a cylindrical conducting resin mold (Buetler Konductomet I, conductive phenolic mounting compound, carbon filled). The sample was then polished mechanically with Struers polishing equipment (RotoPol-31, Roto Force - 4, and Multidoser), first with water and 1200 grit SiC abrasive paper for about 5-10 seconds, and then with $1\mu\text{m}$ monocrystalline diamond solution (Metlab Corp., CAT# M234) on a polishing cloth (Pan W Cloth, Metlab Corp., CAT# M560) for 5-10 minutes. This established a flat sample surface for microprobe analysis. Each sample was coated with a thin layer ($\sim 250\text{\AA}$) of carbon in an evaporating chamber before analysis.

Microprobe analysis was done using a top-loading sample holder which held the specimens flat. At least 10 different 5-10 μm crystallites were analyzed for each sample and averaged to determine the composition. The statistical error was calculated from the standard deviation of the measurements. Additionally, the samples were viewed in composition mode to verify that the materials were generally consistent in composition. Regions which seemed to have different composition were inspected, as one method of determining impurities.

2.3 Results and Discussion

2.3.1 Measured Compositions

The composition of each alloy is shown in Table 2.1. The reported values are an average of the measurements from high-precision microprobe analysis, and the errors are the calculated standard deviations of these measurements. These values were calculated from the atomic ratios by setting $\sum(Mo + Ru) = 6$ for each compound.

The labeling scheme introduced in Table 2.1 will be used throughout the rest of the discussion. Compounds *A1* – *D1* are the alloys made with $Cu_2Mo_6Se_8$, and compounds *A2* – *D2* are the alloys made with “ $Cu_4Mo_6Se_8$ ”. For both series, the *A* samples are the most copper-rich alloys (i.e. $x \approx 0.2$), while the *D* compounds are the least *Cu*-rich alloys (with $x \approx 0.8$). Notice that we use quotation marks around “ $Cu_4Mo_6Se_8$ ”, because previous attempts to synthesis this compound with similar methods resulted in “ $Cu_{3.1}Mo_6Se_8$ ” [4]. The composition of the basic Chevrel compounds used in the alloys have not yet been measured.

The only significant impurities found by microprobe analysis were $MoSe_2$ and a $Mo : Ru$ compound with a ratio for the 4d metals of approximately 1 : 4. During microprobe analysis, it was possible to distinguish these impurities from each other and from the bulk compounds by observation in composition mode. Both impurities were present in each sample, in fairly consistent quantities. We estimate that the samples are 90 – 95% pure, based on observation of the sample surfaces. Although Cu_2Se formed on the surface of the alloys during the final annealing process, we do not see any in the bulk of the samples.

The measured sample compositions generally follow those expected from load-

ing stoichiometry. Within each series of alloys, the amount of Cu decreases from $A \rightarrow D$, while the amount of Ru increases. The measured amount of Se was consistently slightly lower than 8, but is generally within one standard deviation of this expected value, based on the spread of results from the microprobe data. A low Se content seems to be consistent with the small amount of $MoSe_2$ and Cu_2Se impurities formed during synthesis. Alternatively, some studies have shown oxygen substitution on Se sites [11, 12, 13], which could cause low selenium stoichiometries in the Chevrel phase compounds.

A closer inspection of the Cu content in the samples shows that there is consistently slightly less copper than expected from loading. It is likely that most of this ‘missing’ Cu can be attributed to the Cu_2Se formed on the pellet surfaces.

The ruthenium content for most of the samples is within one standard deviation of the expected amount. For samples $A2$ and $B2$, there is slightly less Ru than expected from loading. Again, we attribute these discrepancies to the formation of impurities during synthesis.

Table 2.1: Measured compositions (high-precision microprobe analysis) and unit cell parameters (powder XRD)

Label	Cu	Mo	Ru	Se	$a_H(\text{\AA})$	$c_H(\text{\AA})$	$V_H(\text{\AA}^3)$
$Cu_2Mo_6Se_8$	*	*	*	*	9.962(2)	10.755(2)	924.5(3)
<i>A1</i>	1.5(2)	5.7(5)	0.35(4)	7.7(7)	9.9241(4)	10.740(1)	916.0(1)
<i>B1</i>	1.15(8)	5.2(3)	0.78(6)	7.7(5)	9.8698(5)	10.725(1)	904.8(1)
<i>C1</i>	0.62(4)	4.8(2)	1.19(5)	7.7(3)	9.8157(4)	10.740(1)	896.2(1)
<i>D1</i>	0.21(2)	4.4(1)	1.57(4)	7.7(2)	9.749(1)	10.772(1)	886.6 (2)
“ $Cu_4Mo_6Se_8$ ”	*	*	*	*	10.055(1)	10.727(1)	939.2(2)
<i>A2</i>	2.6(4)	5.7(6)	0.26(3)	7.8(8)	10.009(1)	10.718(2)	929.8(2)
<i>B2</i>	1.7(1)	5.3(2)	0.70(3)	7.7(3)	9.931(1)	10.710(1)	914.7(2)
<i>C2</i>	1.1(1)	4.8(3)	1.2(1)	7.7(5)	9.852(1)	10.705(1)	899.8(2)
<i>D2</i>	0.6(2)	4.4(3)	1.6(1)	7.7(4)	9.769(1)	10.753(1)	888.8(2)
$Mo_4Ru_2Se_8$	*	*	*	*	9.686(1)	10.812(2)	878.5(2)

* not measured

2.3.2 Powder X-ray diffraction analysis

Figure 2.1 shows the powder XRD patterns for series 1, and Figure 2.2 shows the powder XRD patterns for series 2. The calculated peak positions from unit cell parameters are marked with vertical lines below each pattern, and the $MoSe_2$ peaks are marked by arrows above the $Mo_4Ru_2Se_8$ pattern. The patterns within each figure are in compositional order, with the most Cu -rich (i.e. $Cu_2Mo_6Se_8$ or “ $Cu_4Mo_6Se_8$ ”) sample at the bottom, and the most Ru -rich compound, $Mo_4Ru_2Se_8$, at the top. In general, the Ru -rich samples tend to have more $MoSe_2$ impurity, due to the presence of $MoSe_2$ in $Mo_4Ru_2Se_8$.

The $R\bar{3}$ hexagonal unit cell parameters are also shown in Table 2.1. The change in unit cell volume with sample composition varies as expected. V_H gets consistently larger as the amount of Cu increases, and as the amount of Ru decreases. In general, we expect the Chevrel cluster to shrink with the addition of extra electrons when Ru is substituted for Mo [19]. Since more Ru atoms corresponds to more extra electrons, we expect the cluster size to continue to decrease with the addition of more Ru . One may expect a similar correlation with the Cu intercalation, since each copper adds 1 extra electron to the cluster. However, it is likely that intercalated atoms expand the unit cell when filling the (previously) empty sites in the Chevrel network, and thus increase the unit cell volume.

We may also compare the unit cell volumes of these compounds with similar Chevrel phase compounds. For the basic compound Mo_6Se_8 , V_H is 884.4 \AA^3 [14]. As the number of Ru atoms substituted on the Mo octahedra increases, V_H decreases as expected from electronic effects. Previous syntheses of $Mo_4Ru_2Se_8$ have given V_H of 877.4 \AA^3 [15], 879 \AA^3 [16], and 880.5 \AA^3 [17]. These values compare nicely with our value of 878.5 \AA^3 .

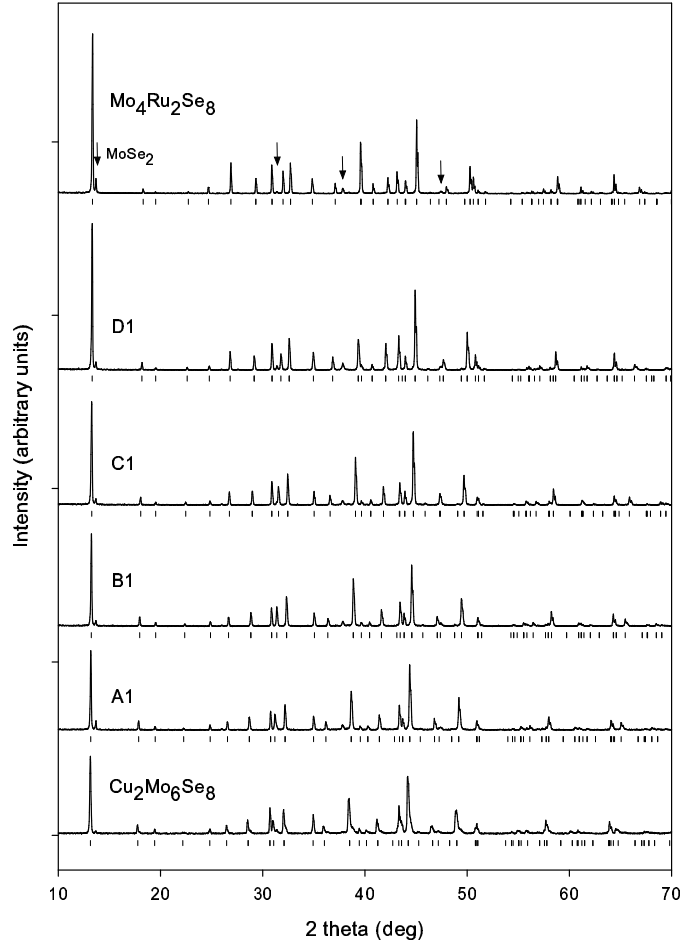


Figure 2.1: Powder XRD patterns for series 1 alloys. See text for details.

Previously reported copper-filled Chevrel phase selenides $CuMo_6Se_8$, $Cu_{1.5}Mo_6Se_8$, and $Cu_2Mo_6Se_8$ have hexagonal unit cell volumes of 899\AA^3 , 908\AA^3 , and 927\AA^3 , respectively [18]. The reported V_H for the Cu_2 compound is similar to that measured in this work (924.5\AA^3). The unit cell volume increases regularly as more Cu is added to the structure. We may also compare our data to comparable sulfide Chevrel compounds. The unit cell volumes of Mo_6S_8 , $Cu_{1.8}Mo_6S_8$, and $Cu_{2.9}Mo_6S_8$ are 797.51\AA^3 [20], 815.36\AA^3 [21], and 838.87\AA^3 [22], respectively. Again, V_H increases with Cu content in a basically linear manner.

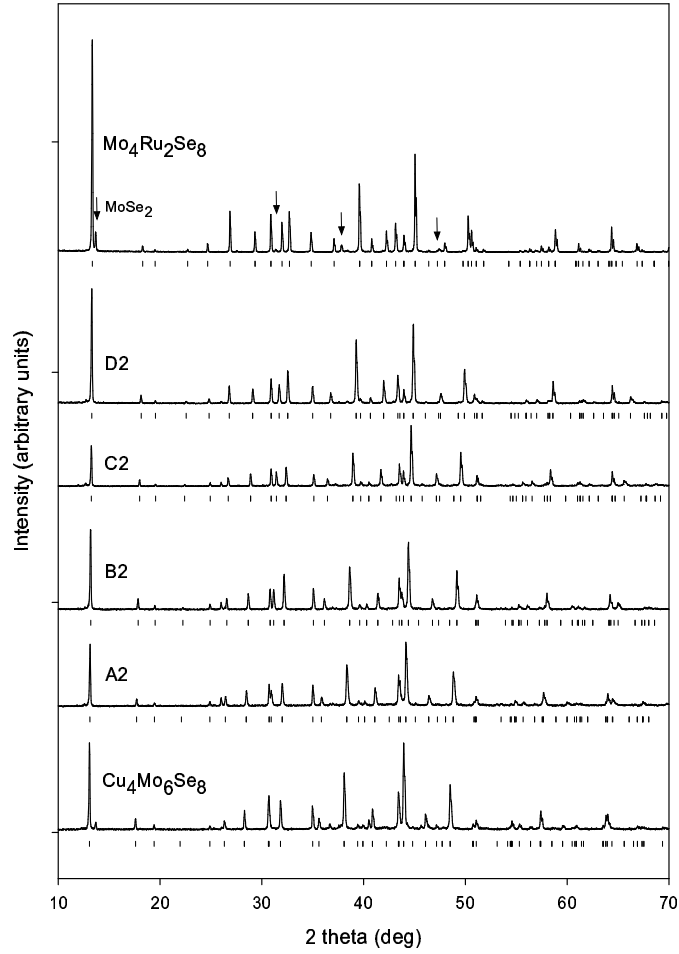


Figure 2.2: Powder XRD patterns for series 2 alloys. See text for details.

2.3.3 Transport property measurements

Resistivity as a function of temperature for series 1 and series 2 compounds are shown in Figures 2.3 and 2.4, respectively. The variation of the Seebeck coefficient with temperature for these samples are shown in Figures 2.5 and 2.6. The data for the $x = 0$ compound shown in the series 2 graphs is from previously published property measurements (of $\text{Cu}_{3.1}\text{Mo}_6\text{Se}_8$) from JPL [4]. The transport property measurements for $\text{Mo}_4\text{Ru}_2\text{Se}_8$ are shown in Figure 2.7. Resistivities below room

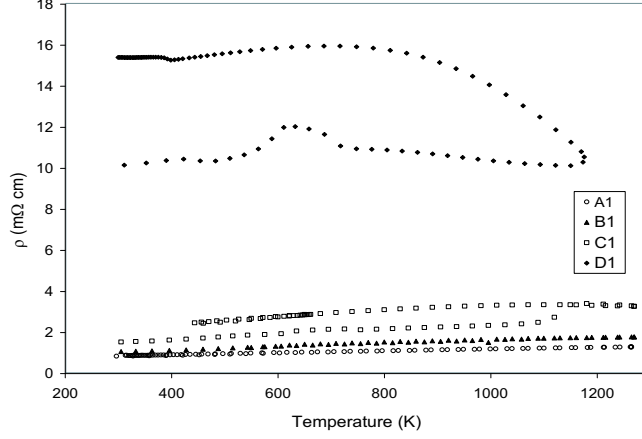


Figure 2.3: Resistivity as a function of temperature for series 1 compounds.

temperature have been previously published for this compound [16].

From these graphs, we see that the $A1 - C1$ and $A2 - C2$ compounds are highly doped semiconductors (or semimetals), which we expect from composition measurements. These compounds have between about $2.2 - 3.8$ extra electrons per cluster, based on the filling of Cu and Ru , which is less than required (by band calculations) to make intrinsic semiconducting Chevrel phases. The resistivity varies nearly linearly with T in these samples, which is typical for metals and highly doped semiconductors. Additionally, ρ is consistently smaller for the compounds with higher Cu filling, as expected. The resistivity and Seebeck measurements of $D1$, $D2$ and $Mo_4Ru_2Se_8$ suggest that they are intrinsic semiconductors. For these compounds, the resistivity decreases with temperature. Particularly in these Ru -rich compounds there is a lot of hysteresis in the measurements.

From the Seebeck measurements, we see that all of the alloys are p-type. However, the $Mo_4Ru_2Se_8$ is an n-type semiconductor for $T \lesssim 1200K$, and p-type above this temperature. Above $600K$, the resistivity of this sample decreases while S increases, which implies that both electrons and holes contribute to the conduction.

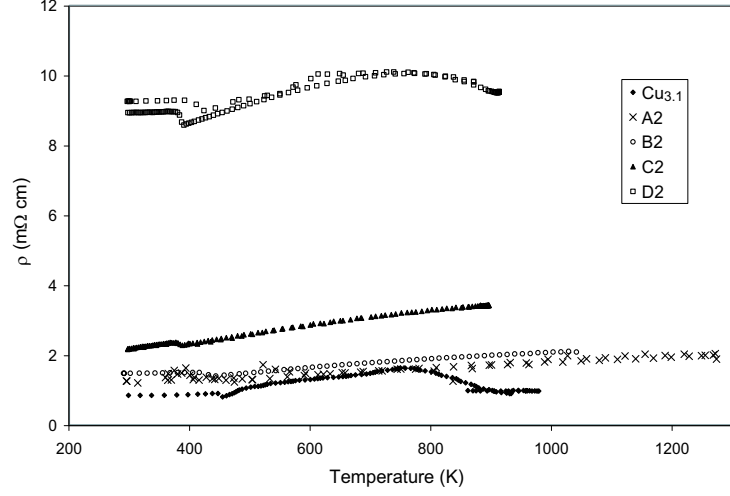


Figure 2.4: Resistivity as a function of temperature for series 2 compounds, and $Cu_{3.1}Mo_6Se_8$ from [4].

This has also been seen in a similar semiconducting Chevrel phase compound, $Mo_4Re_2Se_8$ [23].

A useful parameter for comparison of thermoelectric properties is the power factor, S^2/ρ . Graphs of the power factor as a function of temperature for both series of alloys are shown in Figure 2.8. To make these graphs, a third-order polynomial function was fit to each ρ curve and used to generate new resistivity data at the same temperature as the Seebeck measurements. These calculated resistivity points and the measured Seebeck data were used to calculate the power factor. The power factor for $Cu_{3.1}Mo_6Se_8$ is also shown in each graph for comparison.

As mentioned earlier, $Cu_{3.1}Mo_6Se_8$ is currently one of the best high temperature Chevrel phase TE materials [4], with a rather large power factor and a low thermal conductivity. With $\kappa \sim 15(mW/cm \cdot K)$ at 1000K, this gives $ZT \sim 0.4$ [4]. The Cu - Ru Chevrel alloys presented here generally all have significantly smaller power factors than $Cu_{3.1}Mo_6Se_8$. Assuming similar thermal conductivity, we calculate the best sample, compound $B2$, has $ZT \sim 0.3$ at 1000K. It is not likely

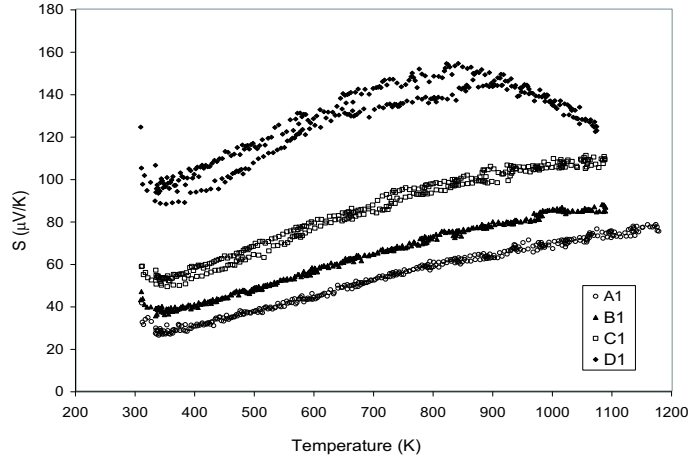


Figure 2.5: Seebeck coefficient as a function of temperature for series 1 compounds.

that the thermal conductivities of these alloys are significantly lower than that of $Cu_{3.1}Mo_6Se_8$, and thus will probably not increase the figure of merit significantly.

2.4 Conclusions

In an effort to find materials with improved high-temperature thermoelectric properties, alloys of $Cu_2Mo_6Se_8$ and “ $Cu_4Mo_6Se_8$ ” with $Mo_4Ru_2Se_8$ were synthesized. These materials were characterized by powder XRD and high-precision microprobe analysis, and their resistivity and thermopower were measured as a function of temperature. The more Cu -rich alloys were found to be highly doped semiconductors (or semimetals), with metal-like resistivity curves, while the most Ru -rich samples and $Mo_4Ru_2Se_8$ were found to be intrinsic semiconductors. Seebeck measurements show that all alloys are p-type semiconductors, and $Mo_4Ru_2Se_8$ changes from n-type to p-type above 1200K. By comparing the power factor of these compounds with $Cu_{3.1}Mo_6Se_8$, we find these materials do not have improved TE properties. However, it is likely that increasing the carrier mobility and decreasing the carrier concentrations would improve these properties considerably.

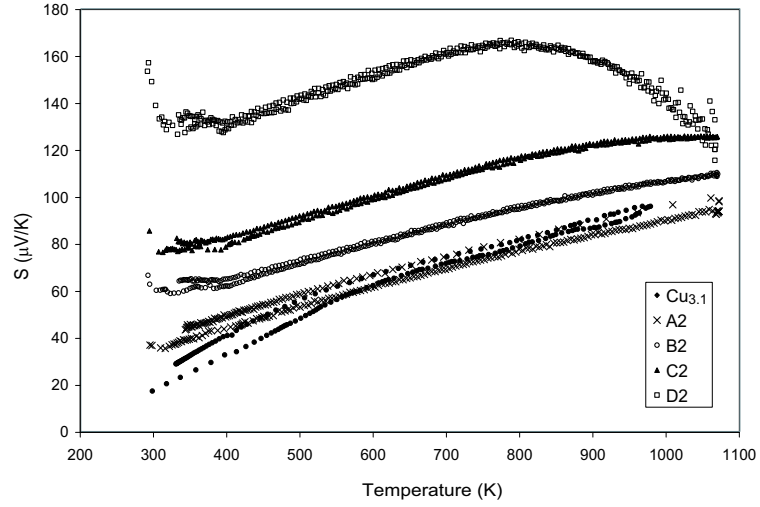


Figure 2.6: Seebeck coefficient as a function of temperature for series 2 compounds, and $Cu_{3.1}Mo_6Se_8$ from [4].

2.5 Acknowledgments

This work was funded by a JPL Grant. I am indebted to Michael McGuire for performing the microprobe analysis. The microprobe and polishing equipment are part of the Cornell Center for Materials Research, which is supported by a MRSEC Grant (DMR-0079992). I would further like to thank Franck Gascoin at JPL for transport properties measurements, and for the $Cu_{3.1}Mo_6Se_8$ data.

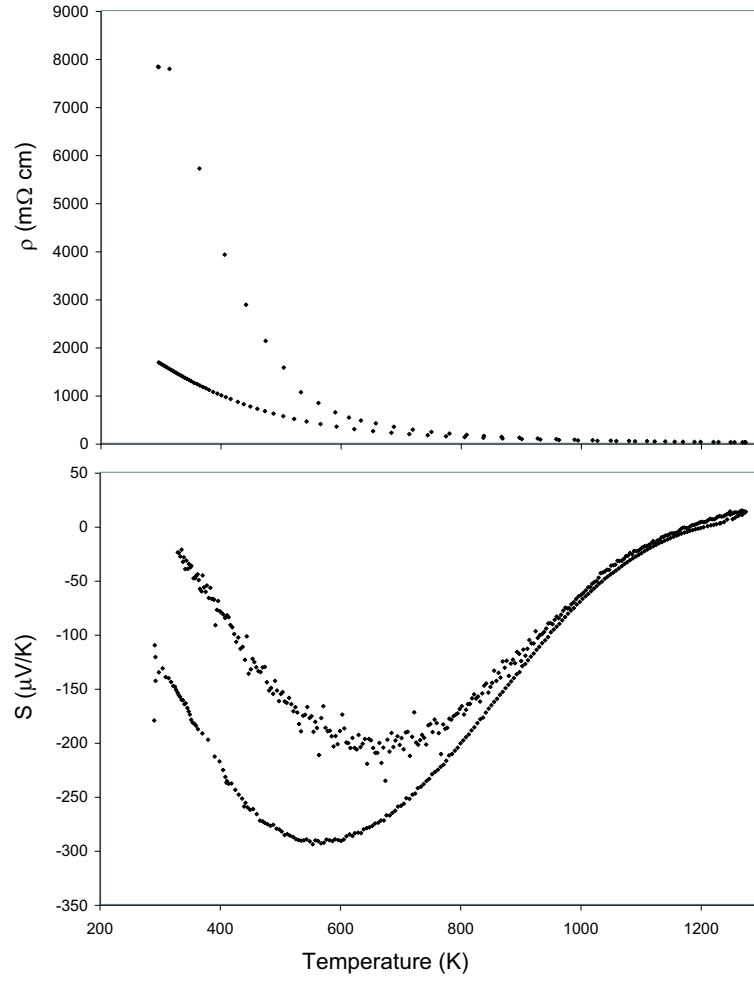


Figure 2.7: Resistivity and Seebeck coefficient as a function of temperature for $Mo_4Ru_2Se_8$.

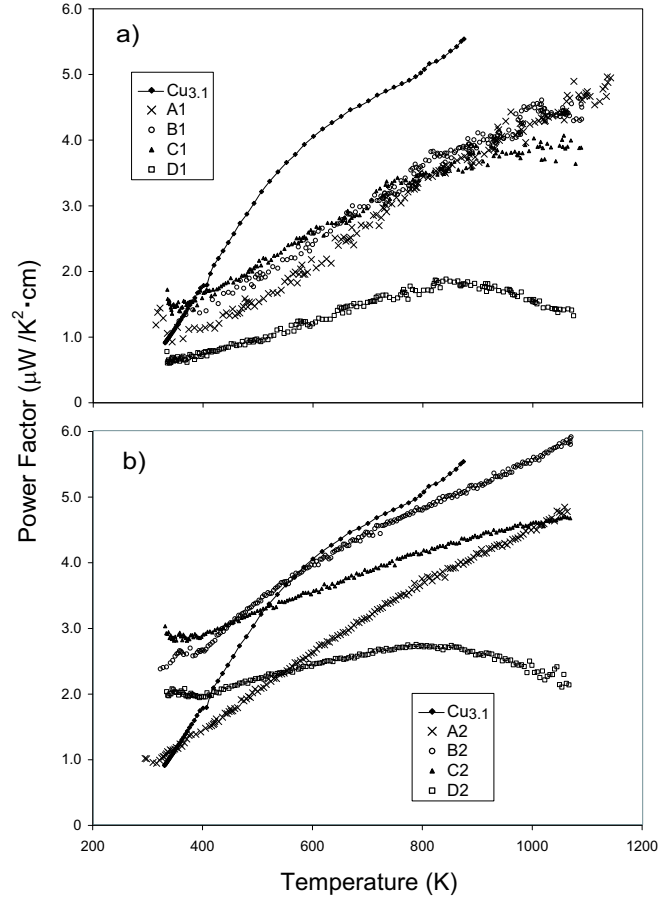


Figure 2.8: Calculated Power Factor as a function of temperature for (a) series 1 and (b) series 2. The Power Factor for $\text{Cu}_{3.1}\text{Mo}_6\text{Se}_8$ from [4] is shown for comparison.

REFERENCES

- [1] A. F. Ioffe, *Semiconductor Thermoelements and Thermoelectric Cooling*, Infosearch Ltd., London (1957).
- [2] G. A. Slack, *CRC Handbook of Thermoelectrics*, chapter 34: New materials and performance limits for thermoelectric cooling, pages 407-440, CRC Press, Inc., Boca Raton, Fl., 1995.
- [3] R. Chevrel, M. Sergent, J. Prigent, *J. Solid State Chem.* **3**, 315 (1971).
- [4] T. Caillat, J. -P. Fleurial, G. J. Snyder, *Solid State Sci.* **1**, 535 (1999).
- [5] G. J. Snyder, T. S. Ursell, *Phys. Rev. Lett.* **91**, 148301 (2003).
- [6] R. W. Nunes, I. I. Mazin, *Phys. Rev. B* **59**, 7969 (1999).
- [7] P. -E. Werner, L. Eriksson, M. Westdahl, *J. Appl. Crystallogr.* **18**, 367 (1985).
- [8] J. A. McCormack, J. -P. Fleurial, *Mat. Res. Soc. Symp. Proc.* **234**, 135 (1991).
- [9] C. Wood, D. Zoltan, G. Stapfer, *Rev. Sci. Instrum.* **56**, 719 (1985).
- [10] J. W. Vandersande, C. Wood, A. Zoltan, D. Whittenberger, *Thermal Conductivity*, Plenum Press, New York (1988).
- [11] C. L. Chang, Y. K. Tao, J. S. Swinnea, H. Steinfink, *Acta. Crystallogr. C* **43**, 1461 (1987).
- [12] D. Guenzburger, et. al., *Phys. Rev. B* **32**, 4398 (1985).
- [13] D. G. Hinks, J. D. Jorgensen, H. -C. Li, *Phys. Rev. Lett.* **51**, 1911 (1983).
- [14] O. Bars, J. Guillevic, D. Grandjean, *J. Solid State Chem.* **6**, 48 (1973).
- [15] L. S. Selwyn, W. R. McKinnon, *J. Phys. C: Solid State Phys.* **20**, 5105 (1987).
- [16] A. Perrin, R. Chevrel, M. Sergent, O. Fischer, *J. Solid State Chem.* **33**, 43 (1980).
- [17] W. Hönle, H. D. Flack, K. Yvon, *J. Solid State Chem.* **49**, 157 (1983).
- [18] K. Yvon, *Curr. Top. Mat. Sci.* **3**, 53 (1979).
- [19] K. Yvon, A. Paoli, *Solid State Commun.* **24**, 41 (1977).
- [20] R. Chevrel, M. Sergent, J. Prigent, *Mat. Res. Bull.* **9**, 1487 (1974).

- [21] K. Yvon, A. Paoli, R. Fluekiger, R. Chevrel, *Acta Crystallogr. B* **102**, 54 (1993).
- [22] K. Yvon, A. Paoli, R. Fluekiger, R. Chevrel, *Acta Crystallogr. B* **33**, 3066 (1977).
- [23] T. Caillat, J. -P. Fleurial, *International Conference on Thermoelectrics*, 16th, chapter New Low Thermal Conductivity Materials for Thermoelectric Applications, pages 446-453 (1997).

CHAPTER 3

SYNTHESIS AND CHARACTERIZATION OF $M_xMo_5RuSu_8$ CHEVREL PHASE COMPOUNDS

In this Chapter we discuss a new set of Chevrel compounds of the type $M_xMo_5RuSe_y$, with $M = Zn, Cd, Sn$ and Pb , $x \lesssim 1$ and $y \approx 8$. The composition of each compound was determined with high-precision microprobe analysis. Furthermore, the structures of the compounds were solved from powder X-ray diffraction using Rietveld refinement. Before we discuss the details of this analysis, we will first review the motivation for studying this series of compounds, as considered in Chapter 1.

3.1 Motivation and review

There has been recent interest in Chevrel phases because of their potential as good high-temperature thermoelectrics [1]. These materials have a ‘rattling’ structure type, which helps to minimize the lattice thermal conductivity κ_l . This may be an important trait for increasing the thermoelectric efficiency [2]. Additional interest in Chevrel phases for use as high temperature thermoelectrics stems from their stability at temperatures greater than $1000^\circ C$.

Chevrel phase materials are based on the Mo_6X_8 structure, where X is a chalcogen (usually S, Se , or Te). The way these units pack leaves empty cavities throughout the structure; and two of these cavities are large enough to provide intercalation sites for a wide range of atoms. It has been found that large atoms like Pb generally fill the larger cavity located at the unit cell origin on the $\bar{3}$ axis, while smaller atoms like Ti and Fe tend to occupy the smaller cavity, or (like Cu) into delocalized sites around the unit cell origin. This intercalation sometimes causes

further distortion of the rhombohedral unit cell, to a lower (triclinic) symmetry, as shown in [3].

The intercalation of various atoms can be used to tune the electrical and thermal properties of Chevrel phase compounds. This is extremely beneficial from a thermoelectric standpoint. It has long been known that semiconductors make the best thermoelectric materials [4]. But Mo_6Se_8 itself is metallic, and requires 4 more electrons to fill the valence band and become semiconducting. These intercalation sites provide an easy way to add electrons to the structure. Additionally, substitution of either Ru or Re for Mo provides another way to add electrons to the system without significantly changing the cluster size or shape. Much work has been done with Chevrel phases of the type $M_xMo_6X_8$, but only a few studies of the mixed transition metal cluster compounds have been reported (see for example [5, 6]). Even fewer investigations combining both intercalation and substitution have been published [7].

The new Chevrel phase compounds reported here incorporate both substitution and intercalation into the Chevrel network. We synthesized materials of the form $M_xMo_5RuSe_8$, with $M = Zn, Cd, Sn$ and Pb , and initial reaction stoichiometries with $x = 1$. Such materials are expected to be semiconducting, since the substitution of one Ru for a Mo atom adds 2 electrons, and the intercalation of one M atom adds another 2 electrons to the Chevrel unit. However, the presence of impurities formed during synthesis change the final stoichiometries of the compounds, affecting the electronic nature of the materials. We present these compounds as important additions to the study of Chevrel phase compounds.

3.2 Experimental analysis

3.2.1 Reagents

To minimize oxygen impurities, the following reagents were reduced in forming gas before use: *Cu* (Fisher Scientific Co., electrolytic powder), *Mo* (Aldrich, 99.9% purity, -100 mesh), and *Ru* (Cerac, 99.95% purity, -325 mesh). This reduction involved placing each powder separately in uncovered alumina crucibles inside a glass tube in a flow-through furnace. The *Cu* powder was heated from room temperature to 300°C over 1 hour, held there for 3 hours, and allowed to cool back to room temperature naturally (i.e with the furnace turned off). The *Mo* and *Ru* powders were heated to 1000°C over 5 hours, held at that temperature for 30 hours, and allowed to cool naturally. After reduction these powders were transferred to an argon-filled glove box without exposure to air. These materials were weighed inside the glove box to prevent oxidation.

Each of the metal *M* elements (*Zn*, *Cd*, *Sn*, *Pb*) were filed from a high purity rod (99.99% or better) inside the argon-filled glove box, also to minimize oxygen in the system.

Se (99.9% purity, 4mm pellets) was used as received.

3.2.2 Sample preparation

First we synthesized Mo_5RuSe_8 , by deintercalating $\text{CuMo}_5\text{RuSe}_8$ with iodine in acetonitrile following the procedure detailed in Tarascon et al. [8]. The $\text{CuMo}_5\text{RuSe}_8$ itself was synthesized by mixing stoichiometric amounts of the elements and sealing them in an evacuated quartz ampoule, then heating it to 400°C over 1 day, holding it there for 1 day, and letting it cool naturally. After this

initial reaction, the sample was mixed well by shaking the unopened ampoule, and then heated again to 1100°C over 15 hours, held there for 2 days, and cooled naturally. Then the sample was mechanically ground in an agate mortar and pestle and pressed into a pellet in a hardened steel and tungsten carbide die. The pellet was vacuum-sealed in another quartz ampoule, heated to 1200°C over 1 day, and then annealed for 3 days. It was necessary to perform these last steps (grinding, pressing into a pellet, and annealing at 1200°C) twice to obtain a nearly single phase specimen (as determined by X-ray diffraction). It was not possible to synthesize pure Mo_5RuSe_8 under the above synthesis conditions.

Nearly single phase polycrystalline samples of $M_x\text{Mo}_5\text{RuSe}_8$ were synthesized by annealing stoichiometric amounts of each metal (with $x = 1$) and the previously synthesized Mo_5RuSe_8 . After mixing, each $M\text{Mo}_5\text{RuSe}_8$ sample was sealed in an evacuated quartz ampoule and annealed at various temperatures for different lengths of time. The samples with *Pb*, *Zn*, and *Cd* were heated over 16 hours from room temperature to 620°C , 350°C , and 250°C , respectively¹. They were held at these temperatures for 7 days and allowed to cool naturally. The *Sn* sample was heated to 500°C over 12 hours, and then annealed for 3 days and allowed to cool². After the first anneal, the *Pb*, *Sn*, and *Zn* samples were ground and pressed into pellets, then re-annealed at the same temperatures to improve sample purity. The *Cd* sample did not require further annealing. Although the *Pb* and *Sn* samples showed little change in their powder XRD patterns after the second anneal, the

¹The annealing temperatures were chosen for each sample so that the vapor pressure of the metal would be at least 10^{-3} torr, which is high enough to ensure contact between the reactants.

²This annealing temperature for *Sn* is much lower than the temperature corresponding to a vapor pressure of 10^{-3} torr. We found at higher temperatures the amount of impurities produced by annealing was greatly increased.

Zn sample did improve significantly.

At the end of the annealing processes, the only significant impurity phase found in any sample was $MoSe_2$. An inspection of the powder patterns show that this phase was formed in the synthesis of Mo_5RuSe_8 , and did not measurably increase during the $M_xMo_5RuSe_8$ syntheses.

3.2.3 Powder X-ray diffraction analysis

After synthesis, the samples were first characterized using powder X-ray diffraction (XRD). The data were collected with a Scintag 2000 theta-theta diffractometer, using $Cu K\alpha$ radiation ($\lambda = 1.54059\text{\AA}$, 45kV, 40mA). Each sample was ground finely with an agate mortar and pestle before the scan. Initially, only short (30 min) XRD scans were taken to determine weather the sample needed further annealing. A sample containing less than 10 weight % impurity was deemed sufficiently pure. These initial XRD scans were made for 2θ from $10 - 70^\circ$, in continuous mode with a step size of 0.02° and a rate of 2 deg/min.

The powder pattern for each finished specimen was then used to determine the unit cell parameters. Each powder pattern was indexed with TREOR software [9]. The calculated parameters were used to investigate possible impurities in the samples, and as a starting point for Rietveld refinement. More than 20 Bragg peaks were used to index each sample.

Finally, long (13.75 hr) powder XRD scans were taken for Rietveld refinement. For these scans the samples were mixed with Si powder (X-Ray Diffraction Accessories, 99% purity, -325 mesh) for an internal standard. The 2θ range was from $10 - 130^\circ$. Data was taken in step mode, with a step size of 0.02° and 8 seconds counting time.

3.2.4 Microprobe analysis

The elemental composition of the samples was determined by high-precision microprobe analysis using a JEOL 8900 electron microprobe and pure metal standards. To prepare the samples for this analysis, a small sample of powder was placed at the bottom a cylindrical mold, and covered with Fast Cure Polyester Resin (Metlab Corp., CAT# M147) which was allowed to harden at room temperature for several days. The surface was then polished mechanically with Struers polishing equipment (RotoPol-31, Roto Force - 4, and Multidoser), first with water and 1200 grit SiC abrasive paper for about 5-10 seconds, and then with $1\mu m$ monocrystalline diamond solution (Metlab Corp., CAT# M234) on a polishing cloth (Pan W Cloth, Metlab Corp., CAT# M560) for 5-10 minutes. This established a smooth sample surface for microprobe analysis. Each sample was then coated with a thin layer of carbon ($\sim 250\text{\AA}$) in an evaporator chamber before analysis.

Microprobe analysis was done using a top-referenced sample holder which held the specimens flat, using an accelerating voltage of 15kV and a current of 20-25 nA. At least 10 different 5-10 μm diameter crystallites were analyzed for each sample and averaged to determine the composition. The error was calculated from the standard deviation of the measurements. Additionally, the samples were viewed in composition mode to verify that the materials were fairly consistent in composition. Regions which seemed to have different composition were inspected and used as one method of determining the composition and identity of low levels of impurities in the sample.

3.2.5 Rietveld refinement

Rietveld Refinement was done with the program FULLPROF [10]. Three phases were refined in each sample, $M_xMo_5RuSe_8$, Si , and $MoSe_2$. The starting positions of the Chevrel phase atoms were taken from $InMo_6Se_8$ [11], which has a similar structure to the Chevrel phase materials reported here (with In located at the unit cell origin). The initial Si parameters were taken from published data [12], and the $MoSe_2$ parameters were taken from a previous refinement.

The TREOR unit cell parameters for each Chevrel phase sample were used for initial refinement. The occupancy of each atom was first set to the nominal atomic compositions, and the M atom occupancies were later refined.

For each Rietveld refinement, there were more than 24 parameters refined, including: zero point, scale, atom positions, isotropic thermal parameters for each atom, U, V, and W (only for Chevrel and $MoSe_2$ phases), unit cell parameters, preferred orientation (only for $MoSe_2$), peak shapes, and two asymmetry parameters.

3.3 Results and Discussion

3.3.1 Measured compositions

The composition of each compound was measured by high-precision microprobe analysis. However, the composition of Mo_5RuSe_8 was not measured directly, but was found by analysis of the $CuMo_5RuSe_8$ sample. We found the actual composition to be $Mo_5RuSe_{7.7}$. Here, the $Mo/Ru : Se$ ratio of the Chevrel material differs from the expected 6:8 probably due to the $MoSe_2$ formed during synthesis and/or to possible oxygen substitution on 3.8% of the Se sites. Oxygen could have entered

the system during the high temperature annealing in silica ampoules. The presence of oxygen was investigated with wavelength dispersive spectroscopy (WDS) on the $CuMo_5RuSe_8$ sample, but no obvious trace was found. It is possible that the amount of oxygen in these compounds is too small to detect with this method.

Previous studies of the effect of oxygen the Chevrel phase compound $SnMo_6Se_{8-x}O_x$ report that the electronic structure is not significantly altered by the substitution of oxygen in the selenium site [13]. The oxygen substitution generally occurs at the $Se(2)$ site, located on the c -axis. This substitution subsequently strains the Chevrel structure with large M atoms at the origin, since these M atoms move away from the origin to complete the shorter O bonds [14, 15]. It has been suggested that for Chevrel phases with smaller M not located at the unit cell origin, the O substitution may occur more readily, since it does not create as much strain on the crystal structure [14]. This supports the possibility of oxygen substitution occurring during the high-temperature synthesis of $CuMo_5RuSe_8$.

The measured stoichiometries of the $M_xMo_5RuSe_8$ Chevrel phases are: $Zn_{0.3}Mo_{4.9}Ru_{1.1}Se_{7.6}$, $Cd_{0.9}Mo_{4.9}Ru_{1.1}Se_{7.7}$, $Sn_{0.7}Mo_{4.9}Ru_{1.1}Se_{7.7}$, and $Pb_{0.8}Mo_{4.9}Ru_{1.1}Se_{7.6}$. These were calculated from the atomic ratios, keeping the sum of the stoichiometric coefficients of $Mo + Ru$ equal to 6. The average atomic ratio and standard deviation for the intercalation stoichiometry in the filled Chevrel phases are shown in Table 3.2. Again we see that the $Mo/Ru : Se$ ratios differ from expected, also probably a result of the $MoSe_2$ and oxygen present in the samples. The consistent stoichiometry of the Se in all the filled compounds suggests that it does not change significantly with filling. Additionally, the deviation from 5:1 for the $Mo : Ru$ stoichiometry is partly determined by the ‘loss’ of Mo to the $MoSe_2$ impurity. However, the scatter in the $Mo : Ru$ ratio from microprobe

measurements of different crystallites is larger than the 0.1 difference from the loaded stoichiometry.

In addition to $MoSe_2$, very small amounts of impurities also adhered to the quartz tubes after the reactions (but often without significant presence in the bulk samples themselves). We estimate that approximately 5% of the Cd metal used in the initial synthesis sublimed to the top of the tube during the annealing process. Furthermore, $PbSe$ and $PbSe_2$ were found in the quartz tubes used to anneal the Pb sample, and some $SnSe$ was present in the Sn ampoule. There was also a small amount of MoO_2 found in the Sn sample. Low intensity Bragg peaks corresponding to these impurities were seen in the corresponding powder patterns, and their presence was also verified using semiquantitative energy-dispersive X-ray spectrometry (EDX) on the sublimed materials.

The Zn filling clearly deviates the most with $x = 0.3$, less than one-third of the expected filling. As such, it is important to note that during the composition analysis a few regions gave compositions with $x \sim 1.5$. These regions looked different than the rest of the matrix when viewed in composition mode, and seemed to have a very small surface area. Additionally, there are no extra Chevrel peaks present in the powder pattern, which we would expect for two such distinct compositions. As a result, we believe this to be a very minor phase in the sample. However, it is significant because it helps explain the disagreement in the measured and expected composition. It is likely that the remainder of the ‘missing’ Zn formed some sort of amorphous phase that is undetectable by XRD.

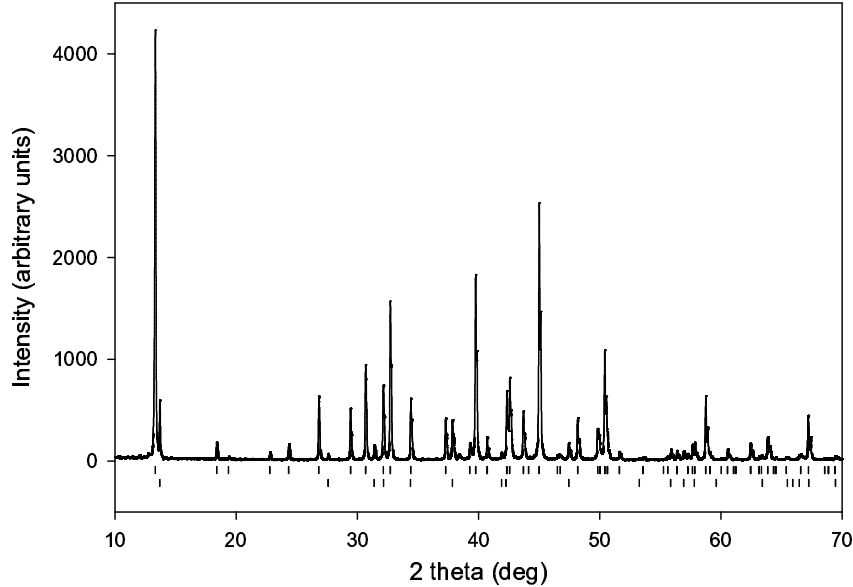


Figure 3.1: Powder XRD pattern of $Mo_5RuSe_{7.7}$, with data from a 30 minute scan. The $Mo_5RuSe_{7.7}$ peak positions are marked by vertical lines directly below the powder pattern, and the $MoSe_2$ peak positions are marked below these. The (002) peak for $MoSe_2$ near 13° is enhanced in intensity due to preferred orientation of this layered phase.

3.3.2 Mo_5RuSe_8 structure

An XRD powder pattern for $Mo_5RuSe_{7.7}$ is shown in Figure 3.1. Except for the peaks pertaining exclusively to $MoSe_2$, and one small unidentified impurity at $2\theta = 38.4^\circ$, all Bragg peaks were indexed.

All $M_xMo_5RuSe_8$ compounds discussed here crystallize in the $R\bar{3}$ space group, and can be defined by hexagonal or rhombohedral unit cells. The $Mo_5RuSe_{7.7}$ hexagonal unit cell was indexed with TREOR, giving $a_H = 9.641(1) \text{ \AA}$, $c_H = 10.968(1) \text{ \AA}$, and a unit cell volume $V_H = 882.9(2) \text{ \AA}^3$. The numbers in parenthesis show the error in the last digit. From these, the rhombohedral unit cell parameters

were calculated, such that $a_R = 6.66 \text{ \AA}$ and $\alpha_R = 92.75^\circ$. All of these parameters compare nicely with those reported for Mo_5RuSe_8 by Selwyn and McKinnon [7], who give rhombohedral parameters $a_R = 6.659 \text{ \AA}$ and $\alpha_R = 92.73^\circ$, and hexagonal parameters $a_H = 9.638 \text{ \AA}$, $c_H = 10.971 \text{ \AA}$ and $V_H = 882.5 \text{ \AA}^3$. We can also compare these with the rhombohedral unit cell parameters for Mo_6Se_8 , which are $a_R = 6.658 \text{ \AA}$ and $\alpha_R = 91.58^\circ$ [16]. Since the parameters for Mo_6Se_8 are very similar to those found for Mo_5RuSe_8 , we verify that the substitution of a Ru atom for one of 6 Mo atoms does not greatly affect the shape or structure of the Chevrel unit.

We may also compare the unit cell volumes of similar Chevrel materials. The hexagonal unit cell volume for Mo_6Se_8 is 884.4 \AA^3 [16], and for $Mo_4Ru_2Se_8$, $V_H = 880.5 \text{ \AA}^3$ [17]. Our measured result for Mo_5RuSe_8 falls directly in between these, as expected. We see that the substitution of Ru for Mo decreases the volume of the unit cell in a regular way. This is expected from electronic effects, since the orbitals filled by the added electrons leave some bonding character [18] and since Ru is slightly smaller than Mo .

3.3.3 Rietveld refinement

The results of the Rietveld refinements for each $M_xMo_5RuSe_8$ compound are discussed below. Figure 3.2 shows the complete powder pattern of each refined compound, which includes the measured intensity counts, the calculated pattern, the difference pattern, and the peak positions of each refined phase. Table 3.1 gives the refined unit cell parameters (hexagonal and rhombohedral), the reliability factors of each calculation, and the weight percent $MoSe_2$ present in each powder pattern. Additional information is given in Table 3.2, which shows the calculated

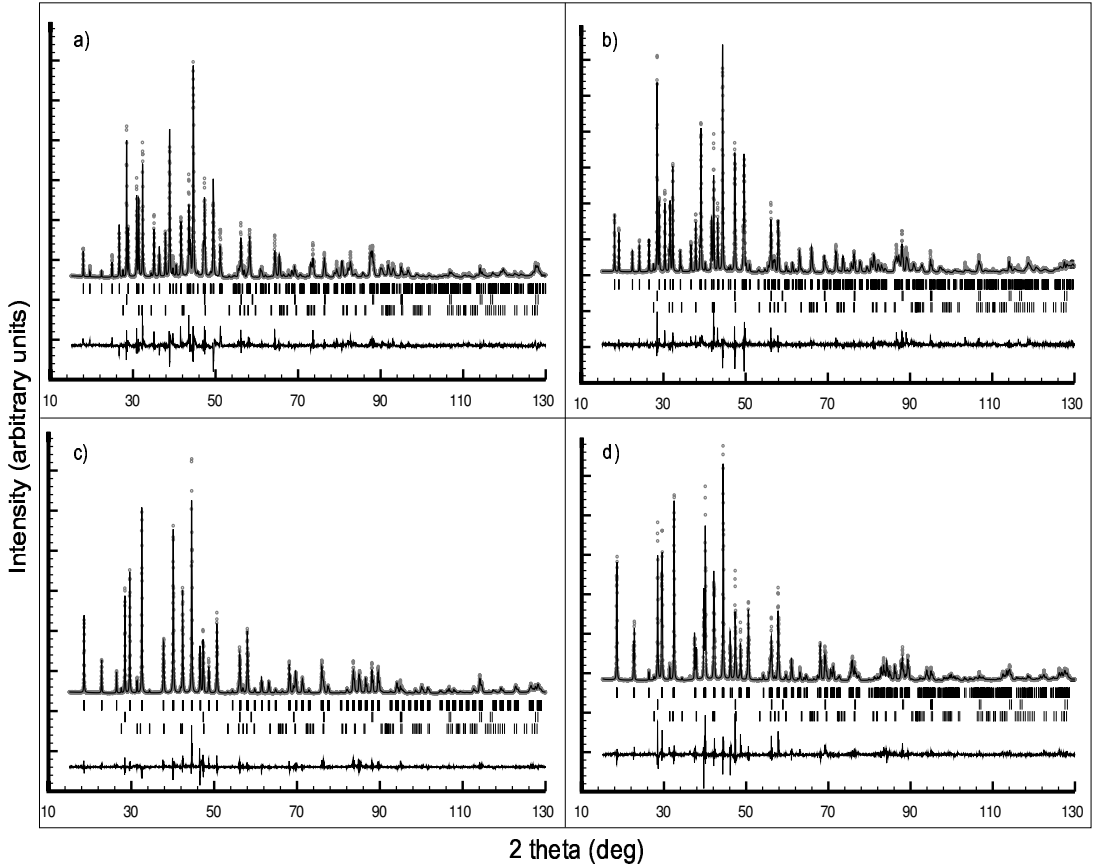


Figure 3.2: Powder patterns for a) $ZnMo_5RuSe_8$, b) $CdMo_5RuSe_8$, c) $SnMo_5RuSe_8$, and d) $PbMo_5RuSe_8$ (nominal compositions). Each pattern shows the measured intensity (grey dots), calculated pattern (overlaid black line), and difference between these (black line at bottom). The vertical lines beneath the powder patterns correspond to the peaks of each refined phase; these include the Chevrel phase compound, Si , and $MoSe_2$ from top to bottom.

atomic positions and thermal parameters from the Rietveld refinement, as well as the atomic ratios measured from the microprobe analysis.

All results reported in Table 3.1 were calculated in FULLPROF, except the rhombohedral unit cell parameters which were calculated from the corresponding hexagonal parameters. The standard deviations for the results are shown in parenthesis, and correspond to the error in the last digit. The errors for a_H and c_H were calculated in FULLPROF, and the error in V_H was calculated with error propagation.

Table 3.1: Refined M occupancy, unit cell parameters, conventional reliability factors, and weight % $MoSe_2$ from the Rietveld method

	MMo_5RuSe_8			
	$M = Zn$	$M = Cd$	$M = Sn$	$M = Pb$
<i>Refined M occupancy</i>	–	0.84	0.73	0.82
<i>Lattice Parameters</i>				
$a_H(\text{\AA})$	9.8748(2)	9.7958(2)	9.5269(1)	9.5407(1)
$c_H(\text{\AA})$	10.7134(3)	11.0561(2)	11.6917(3)	11.8004 (3)
$V_H\text{\AA}^3$	904.71(4)	918.79(3)	918.99(3)	930.19(3)
$a_R(\text{\AA})$	6.73	6.75	6.74	6.77
$\alpha_R(\text{\AA})$	94.44	93.03	89.92	89.63
<i>Reliability factors</i>				
$R_{Bragg}(\%)$	11.1	8.99	7.74	7.10
$R_p(\%)$	20.9	16.5	15.8	17.3
$R_{wp}(\%)$	23.5	18.9	18.6	20.1
$R_{exp}(\%)$	4.78	5.07	4.69	4.67
S	4.9	3.7	4.0	4.3
weight % $MoSe_2$	6.9	8.1	6.8	5.1

$R_p = 100 \sum |y_{obs} - y_{calc}| / \sum |y_{obs}|$; $R_{wp} = \left[100 \sum w |y_{obs} - y_{calc}|^2 / \sum w y_{obs}^2 \right]^{1/2}$;
 $R_{exp} = 100 [N - P / \sum w y_{obs}^2]^{1/2}$; $R_B = 100 \sum_k |I_k - I_{calc,k}| / \sum |I_k|$; $S = R_{wp} / R_{exp}$;
 $w = 1/\sigma^2$; $N - P$ is the number of degrees of freedom.

The refined occupancies of *Cd*, *Sn* and *Pb* are all within one standard deviation of the compositions measured by microprobe. However, although the *Sn* and *Pb* converged well upon refinement, the refinement of the *Cd* occupancy initially gave an unphysical (negative) isotropic thermal parameter. Particularly for the off-origin *M* atoms, the isotropic thermal parameters tend to be quite large but without strong effect on the atom position. As a result, we fixed B_{iso} at 2.5 (\AA^2) for the *Cd* compound, based on the thermal parameters of the *Sn* and *Pb* compounds.

It can be seen from the table that the unit cell increases as the atomic radius of the intercalated *M* atom increases. This is easily seen by inspection of V_H or a_R . Notice that since *Cd* and *Sn* are very similar in size, their unit cell parameters are nearly identical.

It is useful to compare these refined parameters with those found for similar Chevrel compounds. The hexagonal unit cell volume of Mo_6Se_8 is 884.4 \AA^3 [16], and similarly increases as larger *M* atoms are intercalated. V_H reported for compounds of $M_xMo_6Se_8$ with $M_x = Zn, Cd, Sn_{0.8},$ and $Pb_{0.8}$ (in \AA^3) are 909.7 [19], 923.1 [19], 927.7 [20] and 939.6 [20], respectively. These are all slightly higher than the equivalent $M_xMo_5RuSe_8$ compounds, as expected since the molybdenum octahedra shrinks with the addition of extra electrons. Also note that the lower filling fraction of the metals (with $x \lesssim 1$) in the Mo_5RuSe_8 -based compounds likely effects these relations. For $Sn_xMo_6Se_8$ compounds, as the filling fraction of *Sn* gets smaller, V_H is also reduced [20]. This correlation probably holds for these $M_xMo_5RuSe_8$ compounds as well.

It is also interesting to consider the change in α_R in association with different metals intercalated into the Mo_5RuSe_8 structure. Selwyn and McKinnon [7] argue that Chevrel phases which contain large transition metals typically have small

$\alpha_R \sim 88 - 93^\circ$. They note that these small rhombohedral angles usually imply the intercalated atom fills the largest cavity in the Chevrel structure, which is located at the origin of the unit cell. When a filled Chevrel phase has $\alpha_R > 93^\circ$, however, it generally implies that the filling atom is no longer at the unit cell origin. In this case, the large cavity on the 3-fold axis can be delocalized into six smaller sites that form a ring around the unit cell origin. The intercalated atom is generally either located in these sites, or in one of the two smaller cavities created by the packing of the Chevrel phase units. We later show that for the *Cd* compound, which has $\alpha_R > 93^\circ$, the metal atoms are indeed located in these smaller sites.

Next, we would like to discuss the reliability factors reported in Table 3.1. Although these calculated reliability factors are somewhat large, we believe they are not unreasonable for three-phase samples. In each compound, the *MoSe₂* gave the highest R_{Bragg} of all the phases (generally 11-12%). This large R_{Bragg} is likely due to significant preferred orientation of the *MoSe₂* and the non-flat layers. Although there is less than 10 weight% *MoSe₂* in each compound, it increases the overall reliability factors (R_p , R_{wp} , R_{exp} , and thus S). As such, we believe these are factors are not accurate measures of the Chevrel phase refinement, and instead rely on the R_{Bragg} values which correspond to only the Chevrel phase peaks. From this, we conclude the refinement calculations are satisfactory.

Table 3.2 shows the atom positions in the Chevrel compounds in terms of fractional atomic coordinates x , y , and z . Notice that there are two selenium sites, *Se*(1) and *Se*(2); the latter is located on the c-axis. Also shown in Table 3.2 is the isotropic displacement thermal parameter B_{iso} , which was refined separately for the different atoms types (keeping *Se*(1) and *Se*(2) the same, and *Mo* and *Ru* the same). The reported errors were calculated in FULLPROF. All values given

Table 3.2: Positions (x, y, z) and isotropic thermal parameters (B_{iso}) from Rietveld refinement, and atomic ratios from microprobe analysis

nominal comp	atom	x	y	z	B_{iso} (\AA^2)	atm ratio
<i>ZnMo₅RuSe₈</i>	Zn	*	*	*	*	0.3 (1)
	Mo	0.0164(1)	0.1647(2)	0.3986(2)	.63(4)	4.9(5)
	Ru	0.0164(1)	0.1647(2)	0.3986(2)	.63(4)	1.1(1)
	Se(1)	0.3197(4)	0.2839(3)	0.4063(4)	1.22(6)	5.7(5)
	Se(2)	0.000	0.000	0.2081(5)	1.22(6)	1.9(2)
<i>CdMo₅RuSe₈</i>	Cd	0.083(4)	0.085(4)	0.003(2)	2.5 ^a	0.9(1)
	Mo	0.0142(2)	0.1655(2)	0.3998(2)	0.24(3)	4.9(3)
	Ru	0.0142(2)	0.1655(2)	0.3998(2)	0.24(3)	1.1(1)
	Se(1)	0.3194(3)	0.2835(3)	0.4116(3)	0.67(5)	5.8(4)
	Se(2)	0.000	0.000	0.2200(4)	0.67(5)	1.9(1)
<i>SnMo₅RuSe₈</i>	Sn	0.000	0.000	0.000	3.1(3)	0.7(1)
	Mo	0.0149(3)	0.1700(3)	0.4041(2)	0.51(4)	4.9(3)
	Ru	0.0149(3)	0.1700(3)	0.4041(2)	0.51(4)	1.1(1)
	Se(1)	0.3295(4)	0.2931(3)	0.4160(3)	0.74(6)	5.8(4)
	Se(2)	0.000	0.000	0.2385(6)	0.74(6)	1.9(1)
<i>PbMo₅RuSe₈</i>	Pb	0.000	0.000	0.000	2.3(1)	0.8(1)
	Mo	0.0150(3)	0.1696(3)	0.4043(2)	0.53(4)	4.9(5)
	Ru	0.0150(3)	0.1696(3)	0.4043(2)	0.53(4)	1.1(2)
	Se(1)	0.3275(4)	0.2917(3)	0.4159(3)	0.75(6)	5.7(6)
	Se(2)	0.000	0.000	0.2424(5)	0.75(6)	1.9(2)

* see text

^a B_{iso} fixed at this value.

here were obtained while simultaneously refining the M occupancy.

In order to determine the effectiveness of the refinement, each compound was also refined with the M atom removed. This had a large effect on the Cd , Sn , and Pb compounds, causing R_{Bragg} to increase by approximately 80%, 130%, and 315%, respectively. We see that, as expected the heavier metal atoms have a greater influence on the powder pattern. The Zn had very little effect on the refinement, and only changed R_{Bragg} by about 5%.

The Cd atoms are displaced from the origin, while the larger Sn and Pb atoms are located at the origin. Although each filling atom was initially placed at the origin, the B_{iso} value for Cd at this position is extremely large and unphysical even when the occupancy was fixed using the microprobe measurements. Furthermore, we already expect the Cd atoms to be located in smaller sites based on their ‘large’ rhombohedral angles ($> 93^\circ$). Allowing Cd to move off the origin reduced B_{iso} from 28 to 1.1 \AA^2 (with fixed occupancy), and lowered the reliability factors slightly. Thus we believe that Cd is displaced from the origin, and occupies delocalized sites around the 3-fold axis.

These methods were also used for the Zn compound. Allowing Zn to occupy the delocalized positions near the origin did improve the reliability factors, but were not effective in reducing B_{iso} . This value was fixed at 2.5 \AA^2 for further calculations, but the refinement still would not converge. Attempts to place the Zn in several alternate locations gave unphysical bond lengths. Due to the low filling fraction of Zn , and its smaller X-ray scattering power, the current methods cannot accurately determine the Zn positions. Indeed, even completely removing the atom from the unit cell has little effect on the reliability factors of the refinement. We are certain that Zn is present in the sample from both microprobe analysis and

calculated lattice parameters, with V_H significantly larger than in the pseudobinary compound.

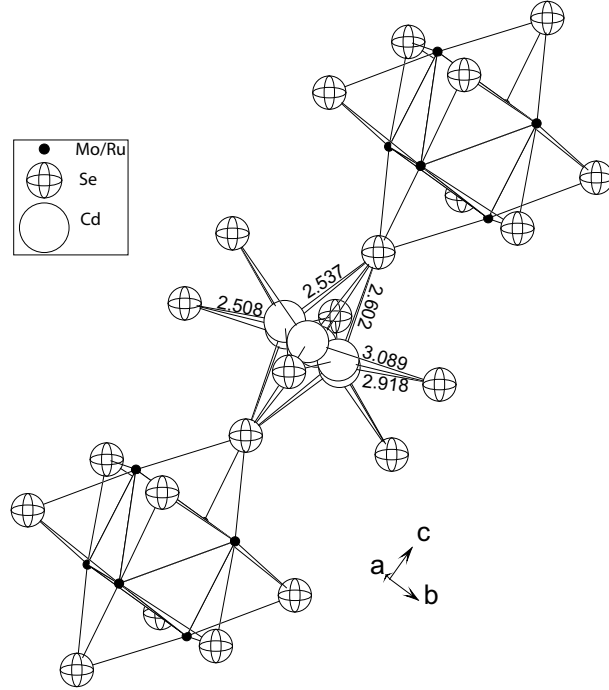


Figure 3.3: $CdMo_5RuSe_8$ structure. Bond lengths are labeled in Angstroms.

3.3.4 Crystal structures

The crystal structures of the filled Chevrel phases are shown in Figures 3.3 and 3.4. Each diagram shows the $M - Se$ bond lengths. Other bond distances will be discussed in the next section.

All compounds have the typical $R\bar{3}$ Chevrel phase structure based on the packing of Mo_6Se_8 units. In each compound, approximately one Ru atom is substituted for a Mo atom in each unit, and is located on the same site.

The Cd site is moved away from the origin, to the general position (x, y, z) , producing six equivalent sites which form a ring around the origin. The Cd atoms are distributed among those six positions. The $Cd-Se(2)$ bond lengths along the

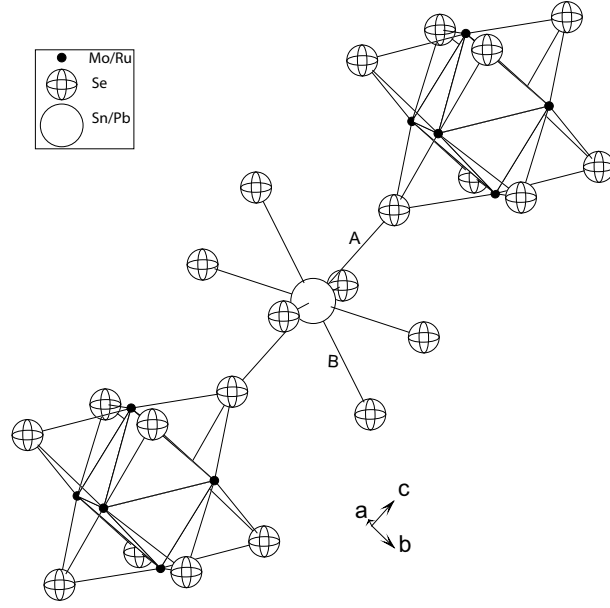


Figure 3.4: $(Sn/Pb)Mo_5RuSe_8$ structure. $M - Se$ bonds are labeled A and B. For Sn , $A = 2.789\text{\AA}$ and $B = 3.189\text{\AA}$. In the Pb structure, $A = 2.861\text{\AA}$ and $B = 3.209\text{\AA}$.

c-axis are 2.537\AA and 2.602\AA , and to $Se(1)$ atoms are 2.508\AA , 2.918\AA and 3.089\AA . These are shown in Figure 3.3. The bonds along the c-axis are comparable to the $Cd-Se$ bond distances in hexagonal ($P63MC$) $CdSe$, which are $2.631 - 2.633\text{\AA}$ [24].

The Sn and Pb atoms both fill the largest cavity at the origin of the unit cell. Because they have such similar structures and only slightly different bond lengths, we present only one diagram for both compounds, in Figure 3.4. Notice that the $M - Se$ bond lengths are slightly larger for the Pb compound, as expected. The $Sn - Se$ bond distances along the c-axis are 2.789\AA , and are otherwise 3.189\AA . We can compare these to $Sn - Se$ bond distances in the orthorhombic ($PNMA$) $SnSe$, which are $2.720 - 3.471\text{\AA}$ [21]. The $Pb-Se$ bond lengths are 2.861\AA along the c-axis, and 3.209\AA otherwise. These bond distances are similar to those in $PbMo_6Se_8$, which vary from $2.895 - 3.205\text{\AA}$ [22]. We also note that the $Pb - Se$

bond lengths in cubic ($FM3 - M$) $PbSe$ are 3.061\AA [23].

3.3.5 Cluster metal and selenium bonds

Table 3.3 gives selected bond lengths for the $M_xMo_5RuSe_8$ compounds and other similar Chevrel phases. The notation and discussion below closely follows that of Berry and Gibbs [25].

An important value to consider for this discussion is the number of extra electrons on each Chevrel unit, beyond the 20 metal-metal boundary electrons in the Mo_6Se_8 cluster. This is calculated as follows: we assign a +6 oxidation state for Mo , which gives each pure Mo_6 octahedra +36 electrons. For all compounds we assume 16 electrons are removed from the Mo/Ru octahedra by the Se and O atoms (which have a formal oxidation state of -2). Then, for each Ru atom substituted on a Mo site, we add 2 extra electrons. And for each metal atom we add $2x$ electrons to the octahedra, since each M has +2 valence electrons.

There are three types of $Mo - Mo$ bonds in the Chevrel structure. The two intra-cluster bond distances are denoted d_1 and d_2 , which are roughly oriented parallel- and perpendicular- to the c-axis, respectively. These are shown in Figure 3.5. The third $Mo - Mo$ distance, d_3 , is the closest intercluster $Mo - Mo$ contact. We also report cluster metal (i.e Mo or Ru) to Se bond lengths. The $Mo/Ru - Se(1)$ intercluster bond length is given first, followed by the average $Mo/Ru - Se$ intracuster bond length. Next we calculate Δ , which is the difference between the average distance of the $Mo/Ru - Se$ intracuster bond of each compound, with that of Mo_6Se_8 . Finally, we show the calculated number of extra electrons (e^-) on each Chevrel unit.

As expected, we see that the Mo/Ru octahedra shrinks as more electrons are

Table 3.3: Selected bond lengths (in Å)

composition	d_1	d_2	d_3	Mo/Ru-Se(1) inter	Mo/Ru-Se intra	Δ	extra e^-
$Mo_6Se_6^g$	2.836	2.684	3.266	2.599	2.563	0.0	0
$Sn_{0.8}Mo_6Se_6^g$	2.755	2.680	3.419	2.694	-	-	1.6
$PbMo_6Se_6^g$	2.734	2.679	3.490	2.772	2.577	0.014	2.0
$Mo_4Ru_2Se_6^g$	2.710	2.659	3.386	2.683	2.540	-0.23	4.0
Mo_5RuSe_8	-	-	-	-	-	-	2.0
$Zn_{0.3}Mo_{4.9}Ru_{1.1}Se_{7.6}$	2.670	2.687	3.460	2.625	2.568	0.005	2.8*
$Cd_{0.9}Mo_{4.9}Ru_{1.1}Se_{7.7}$	2.707	2.696	3.474	2.667	2.548	-0.014	4.0*
$Sn_{0.7}Mo_{4.9}Ru_{1.1}Se_{7.7}$	2.729	2.691	3.433	2.682	2.549	-0.013	3.6*
$Pb_{0.8}Mo_{4.9}Ru_{1.1}Se_{7.6}$	2.739	2.687	3.451	2.702	2.541	-0.023	3.8*

^aBerry and Gibbs [25] *calculated assuming Se vacancies are filled by isoelectronic O.

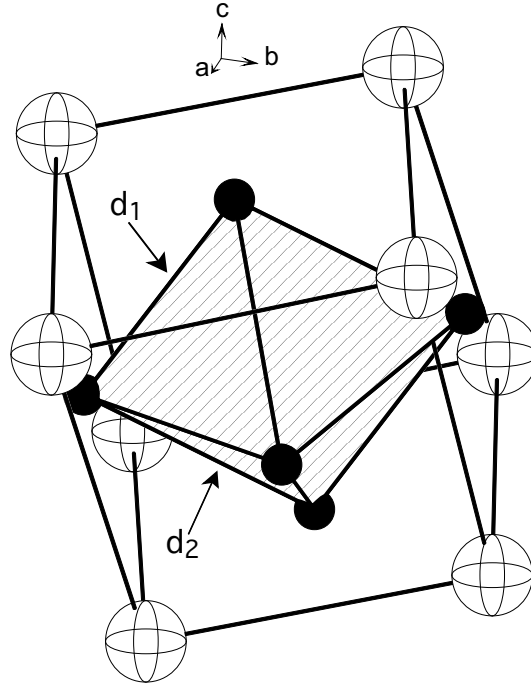


Figure 3.5: Intracluster Mo-Mo bonds in Mo_6Se_8 Chevrel unit, labeled d_1 and d_2 following Berry and Gibbs [25]. The Mo atoms are black, and the Se atoms are crossed.

added. This change is most apparent by inspection of d_1 . We also see by comparison of the $PbMo_6Se_8$ and $Pb_{0.8}Mo_{4.9}Ru_{1.1}Se_{7.6}$ structures that the Ru -substitution lessens this contraction. Berry and Gibbs [25] believe this is because of the increased Lewis acidity of these metal sites, which partly counteracts the contraction of bonds from the electronic effect.

It is also clear from Table 3.3 that the $Mo/Ru - Se(1)$ intercluster bond increases with the addition of extra electrons to the basic Mo_6Se_8 unit, although less so when Ru is substituted. Again, this can be attributed to the increased acidity of the Mo/Ru sites.

Finally, we will discuss the change in the $Mo/Ru - Se$ intracluster bond. It seems that though the addition of electrons tends to increase this distance, the Ru substitution decreases intracluster $Mo/Ru - Se$ bond with respect to Mo_6Se_8 . We

see a net decrease in distance for $Mo_4Ru_2Se_8$ and our $M_xMo_5RuSe_8$ compounds, except the Zn structure which is slightly positive.

3.4 Conclusions

This paper describes the solid-state synthesis and characterization of filled Chevrel phase compounds of the form $M_xMo_5RuSe_8$, with $M = Zn, Cd, Sn,$ and Pb . The composition of each compound was measured with high-precision microprobe analysis, and the structures were characterized with Rietveld refinement. It was found that the compositions differed from the expected stoichiometry in terms of the metal filling fraction, x , as well as the cluster metal-to-selenium ratio, likely due to some oxygen substitution on selenium sites. In general, the structure of the synthesized compounds followed typical arrangement for Chevrel phase materials, with large intercalated atoms filling the large site at the unit cell origin and the smaller metals filling smaller cavities, in this case forming a ring of dislocated sites around the origin. The positions of the M atoms were generally predicted by the calculated rhombohedral angle of the compound, and verified by Rietveld refinement. We find that the refined parameters and calculated bond lengths of the compounds are completely satisfactory, and generally follow our expectations. However, the position of the Zn atom is not known, because of its low scattering power and small effect on the powder pattern. Unfortunately, this group of $M_xMo_5RuSe_8$ compounds will not make good high-temperature thermoelectrics. They are not stable at high temperature, and begin to rapidly decompose between $700-800^\circ C$ into $M, Mo_5RuSe_8,$ and $MoSe_2$. These compounds do, however, form an interesting series of Chevrel phases that combine cluster metal substitution of Ru for Mo with intercalation of different metals.

3.5 Acknowledgments

This work was funded by a JPL Grant. I would also like to thank John Sinnot for guidance with mounting and polishing and John Hunt for assistance with high-precision microprobe techniques. The microprobe and polishing equipment are part of the Cornell Center for Materials Research, which is supported by a MRSEC Grant (DMR-0079992). Finally, I would like to express my appreciation to Mark Bailey for help with the FULLPROF refinements, and Franck Gascoin and G. Jeffrey Snyder for helpful discussions about Chevrel phase materials.

REFERENCES

- [1] T. Caillat, J. -P. Fleurial, G. J. Snyder, *Solid State Sci.* **1**, 535 (1999).
- [2] R. R. Heikes and R. W. Ure, *Thermoelectricity: Science and Engineering*, Interscience, New York (1961).
- [3] R. Chevrel, M. Sergent, *Topics in Current Physics, Superconductivity in Ternary Compounds I*, Springer-Verlag, Berlin, 25 (1982), ed. O. Fisher and M. B. Maple.
- [4] A. F. Ioffe, *Semiconductor Thermoelements and Thermoelectric Cooling*, Infosearch Ltd., London (1957).
- [5] A. Perrin, M. Sergent, O. Fischer, *Mat. Res. Bul.* **13**, 259 (1978).
- [6] A. Perrin, R. Chevrel, M. Sergent, O. Fischer, *J. Solid State Chem.* **33**, 43 (1980).
- [7] L. S. Selwyn, W. R. McKinnon, *J. Phys. C: Solid State Phys.* **20**, 5105 (1987).
- [8] J. M. Tarascon, F. J. DiSalvo, D. W. Murphy, G. Hull, J. V. Waszczak, *Phys. Rev. B* **29**, 172 (1984).
- [9] P. -E. Werner, L. Eriksson, M. Westdahl, *J. Appl. Crystallogr.* **18**, 367 (1985).
- [10] D. B. Wiles, R. A. Young, *J. Appl. Crystallogr.* **14**, 149 (1981).
- [11] A. Lipka, K. Yvon, *Acta Crystallogr. B* **36**, 2123 (1980).
- [12] W. L. Bond, W. Kaiser, *J. Phys. Chem. Solids* **16**, 44 (1960).
- [13] D. Guenzburger, et. al., *Phys. Rev. B* **32**, 4398 (1985).
- [14] C. L. Chang, Y. K. Tao, J. S. Swinnea, H. Steinfink, *Acta Crystallogr. C* **43**, 1461 (1987).
- [15] D. G. Hinks, J. D. Jorgensen, H. -C. Li, *Phys. Rev. Lett.* **51**, 1911 (1983).
- [16] O. Bars, J. Guillevic, D. Grandjean, *J. Solid State Chem.* **6**, 48 (1973).
- [17] W. Hönle, H. D. Flack, K. Yvon, *J. Solid State Chem.* **49**, 157 (1983).
- [18] K. Yvon, A. Paoli, *Solid State Commun.* **24**, 41 (1977).
- [19] E. Gocke, W. Schramm, P. Dolsheid, R. Schöllhorn, *J. Solid State Chem.* **70**, 71 (1987).
- [20] J. M. Tarason, et al., *J. Solid State Chem.* **54**, 204 (1984).

- [21] K. Adouby, C. Perez-Vicente, J. C. Jumas, *Zeitschrift fuer Kristallographie* **213**, 343 (1998).
- [22] J. Guillivec, H. Lestrat, D. Grandjean, *Acta Crystallogr B* **32**, 1342 (1976).
- [23] Y. Noda, et al., *Acta Crystallogr. C* **43**, 1443 (1987).
- [24] Y. -N. Xu, W. Y. Ching, *Phys. Rev. B* **48**, 4335 (1993).
- [25] F. J. Berry, C. Gibbs, *J. Solid State Chem.* **109**, 22 (1994).

CHAPTER 4

CONCLUSION

The widespread use of thermoelectric refrigeration or power generation devices is currently constrained by low efficiencies of the materials. At the present efficiency, thermoelectrics are only useful in niche markets where the benefits of portability, small mass, and minimal vibration are more important than high efficiency. Especially in these markets, even small improvements in the materials efficiency would have a significant impact. The research presented in this thesis was conducted in an effort to find improved high-temperature thermoelectric materials to be used for power generation for instruments on unmanned spacecraft.

Here we look specifically at Chevrel phase materials, based on $M_xMo_6Se_8$ units, which have a rattling structure type that helps to minimize the thermal conductivity. The Chevrel clusters pack in a way that allows the intercalation of various metals into the network. This intercalation, or substitution of Ru , Re , or Rh on some of the Mo sites can be used to make the Chevrel compound semiconducting, which is necessary for good thermoelectric materials. In practice it has been a challenge to make semiconducting Chevrel phases, although there have been a few such compounds reported.

The research presented here involves a combination of substitution of Ru on some of the Mo sites and the intercalation of various metals into the Mo_6Se_8 structure in an attempt to find improved thermoelectric materials. The synthesis and characterization of $M_xMo_5RuSe_y$, with $M = Zn, Cd, Sn$ and Pb , $x \lesssim 1$ and $y \approx 8$ are discussed. These materials will not make improved high-temperature thermoelectric materials, since they begin to decompose at around $700^\circ C$. Additionally, the synthesis and transport property measurements of the Chevrel phase solid so-

lutions $(Cu_yMo_6Se_8)_{1-x}(Mo_4Ru_2Se_8)_x$, with $y = 2, 4$ and $x \approx 0, 0.2, 0.4, 0.6, 0.8$ and 1 are reported. The highest ZT for these materials is ~ 0.3 . Nevertheless, since very few Chevrel phases have been previously synthesized with a combination of substitution and intercalation, this research is an important addition to the study of Chevrel phase compounds.